Applied Ocean Research 142 (2024) 103832

Contents lists available at ScienceDirect

Applied Ocean Research

journal homepage: www.elsevier.com/locate/apor

Research paper

Multiphase SPH analysis of a breaking wave impact on elevated structures with vertical and inclined walls

Krisna Adi Pawitan [a,*], Maria Garlock [a], Shengzhe Wang [b]

[a] Department of Civil and Environmental Engineering, Princeton University, Princeton, NJ 08544, United States
[b] Department of Civil Engineering, University of Colorado Denver, Denver, CO 80217, United States

ARTICLE INFO

Keywords:
Wave structure interaction
Breaking wave impacts
Elevated structure
Smoothed particles hydrodynamics (SPH)
Dualsphysics
Computational fluid dynamics

ABSTRACT

Elevated structures are prevalent along shorelines that are susceptible to storm surge flooding to improve coastal resilience. In this work, we explore the influence of front wall inclination on the pressures and forces attracted by an elevated structure in response to extreme wave impact. Multiphase smoothed-particle hydrodynamics was used to examine a typical two-story building 6 m high and 10 m long with three different frontal wall inclinations impinged by a single breaking wave propagating landwards (from left to right). Relative to a vertical surface, both positive (clockwise) and negative (counterclockwise) inclinations of the front wall altered breaking wave pressures depending on the structure's position relative to the still-water level (SWL). When the bottom of the structure is located below the SWL (negative air gap), a positive inclination decreased breaking wave loads by up to 21 %, while a negative inclination may result in 50 % higher pressure maxima. However, for a structure elevated above the SWL (positive air gap), negative and positive inclinations witnessed reductions to the pressure maxima of 35 % and 10 %, respectively, when compared with a vertical surface.

1. Introduction

The latest Intergovernmental Panel on Climate Change (IPCC) 6th assessment indicates a new high-end risk assessment of 2 m sea level rise by 2100 and 5 m by 2150 due to uncertainty in ice sheet processes (Fox-Kemper et al., 2021). Combined with the increasing likelihood of extreme weather events, such as hurricanes or tsunamis as mentioned in the same report, future coastal structures will need to endure not only higher waves and sea levels, but also short duration local pressures as impact loads due to breaking waves (Wehner et al., 2021). While such impact forces can be 10 – 50 times greater than nonbreaking waves, their millisecond duration has historically promulgated the incorrect assumption that the temporal scale of wave breaking is far too short to cause any structural damage (Oumeraci, 1994).

Recent explorations show that buildings built prior to the updated Flood Insurance Rate Maps (FIRMs) issued by the US Federal Emergency Management Agency (FEMA) were badly damaged during Hurricane Ike (2008) and Hurricane Sandy (2012) (Park et al., 2017). The same study suggested that examining wave loading on elevated structures is key to designing resilient coastal buildings. Separate experiments on non-elevated structures, however, noted that waves breaking directly on the structure produce an impact load that may result in structural failure (Oumeraci, 1994; Peregrine, 2003; Tomiczek et al., 2016a, 2016b). Among the limited references of impact loads resulting from breaking wave impacts, most are looking at the impact force prediction on a vertical wall (Cuomo et al., 2010a, 2010b; Cuomo et al., 2011; Pawitan et al., 2020; Mitsuyasu, 1966; Fuhrboter, 1968; Nagai, 1960). Few were investigating the influence of the front wall's inclination or shape on the impact loads experienced by the structure, especially on an elevated structure.

The complicated interaction between water and entrapped air during wave breaking makes such phenomena difficult to experimentally evaluate. At the model scale, Froude scaling maintains a constant ratio between gravity and inertia forces of the prototype with the reduced scale experiment (Hughes, 1993). Conversely, air compression is primarily governed by the Reynolds number which is incompatible with Froude scaling. Achieving both Froude and Reynolds similitude for the model and prototype necessitates the use of fluids with different viscosities or a dramatic increase in the gravitational acceleration at model scale (e.g., via a centrifuge). Furthermore, wave breaking is a non-linear phenomenon where the peak pressure of wave impact upon a structure changes every time and will depend on the "cleanliness" of the breaking

* Corresponding author.
E-mail address: krisna.pawitan@princeton.edu (K.A. Pawitan).

https://doi.org/10.1016/j.apor.2023.103832
Received 14 August 2023; Received in revised form 26 November 2023; Accepted 30 November 2023
0141-1187/© 2023 Elsevier Ltd. All rights reserved.

wave formed during the experiment. This characteristic is highly influenced by the quality of the water even within a tightly controlled laboratory (Müller and Whittaker, 1993). Due to these difficulties, testing the influence of a front wall's inclination experimentally at model scale will be difficult to achieve consistently and accurately.

Numerous contradictions are reflected in contemporary literature reporting breaking wave impact pressures measured on an inclined wall. Early measurements of breaking wave impact compared a vertical wall with that exhibiting a positive 30° tilt (Richert, 1968), where positive is a clockwise tilt from vertical with the wave approaching from seawards on the left. The results showed a 53 % reduction in peak pressure in comparison to a vertical wall. This result is supported by a subsequent experiment using a positive 15° inclination which resulted in a 22 % reduction of impact pressure when compared with a vertical wall (Whillock, 1987). A more recent study, however, showed contradictory results where a positively inclined wall may increase the pressure relative to a vertical wall (Kirkgöz, 1991). By varying the inclination from −5° to 30°, the peak pressure increased by 1.27 to 1.77 times when compared against a vertical wall. A pressure reduction of 0.54 was only achieved at a positive inclination of 45° (Kirkgöz, 1991). Similar experiments were conducted during the design of a Wave Energy Converter by Queen's University of Belfast located on the Isle of Isla, called the Land Installed Marine Power Energy Transmitter (LIMPET) (Müller and Whittaker, 1993). In this case, the front wall was elevated such that sea water can pass below the lower "lips" of the structure into a closed chamber. The author concluded that changing the wall's inclination will reduce the impact pressure by a factor of 0.62 when it is positively inclined by 32.7° and by a factor of 0.77 when it is negatively inclined by the same angle. These results are consistent with Richert (1968) and Whillock (1987) but in contrast to Kirkgöz (1991).

While physical experimental testing excels in simulating real physical interactions between fluids and complex structures, the implementation of such can be challenging due to scaling effects (Pawitan et al., 2019; Viviano et al., 2018; Cuomo et al., 2010b) and the high cost associated with it. This is why computer aided simulations, such as computational fluid dynamics (CFD), when validated with experiments, can be a viable option to mitigate the cost, while keeping the ability to observe complex wave-structure interaction models. These can employ either Eulerian mesh-based or Lagrangian mesh-free methods. In the Eulerian approach, the fluid is modeled as a continuum and calculated as a discretized control volume within a mesh. Eulerian models are efficient and commonly used for coastal engineering applications involving relatively simple structural geometries without any complex fluid deformation such as breaking waves or sloshing (Suzuki et al., 2017). The limitation of relatively simple geometry comes from the special treatment needed for the free-surface where different fluid phases (usually water and air) interact. Therefore, the simulation of fluid behavior with non-linear multiphase characteristics such as wave breaking or bubble formation is computationally expensive and challenging (Liu et al., 2019; Altomare et al., 2017). In Lagrangian smoothed-particle hydrodynamics (SPH), the fluid is modeled as particles that contain specific properties based on water or air. The particle trajectory at each time step is calculated using the Navier-Stokes equations driven by the number of particles in a given volume (particle density). Since each particle represents a specific type of fluid, motions at the free surface where air and water particles interact can be simulated without special treatments. The simulation is also able to accommodate extreme fluid deformations such as wave breaking or in-chamber sloshing (Guilcher et al., 2013; Lu et al., 2021; Domínguez et al., 2019b).

The SPH method has been increasingly popular over the years for coastal related experiments (Heller et al., 2016; Rogers et al., 2010; Liu and Liu, 2010; Shimizu et al., 2020; Altomare et al., 2022; Sun et al., 2023; Khayyer et al., 2023) and wave energy generation design (Marrone et al., 2019). A previous study utilized the open-source SPH program DualSPHysics (Altomare et al., 2022) to model an elevated structure impacted by tsunami-like waves (Reis et al., 2022). However, the work is limited to single-phase simulations featuring only water particles. Comparisons were made between the simulation and scale-model tests done at Oregon State University. It was found that DualSPHysics was able to simulate both broken and unbroken waves to obtain reasonably accurate force and pressure measurements along the front wall and bottom of the structure. These findings were supported by subsequent research that studied artificial viscosity coefficient (α) as one of the determinant factors in replicating an accurate breaking wave (Roselli et al., 2018; Sato et al., 2021; Altomare et al., 2021, 2023).

While single-phase SPH have been shown to simulate breaking wave very well, Sun et al. (2019) and Lind et al. (2017) argued that the absence of air particles may influence the accuracy of the breaking wave impact pressure experience by a coastal structure, especially during the initial phase when the breaking wave traps an air pocket between the structure. Lind et al. (2017) suggested that differences in pressure between single and multiphase simulations may also arise due to discrepancies between the free-surface profile. Reis et al. (2022) and Marrone et al. (2019) compared 3D with 2D simulations and concluded that 3D models achieve higher accuracy at the cost of 100 to 120 times more computational resources. This gap in accuracy could also be reduced by increasing the 2D wave height to inter-particle distance ratio to at least 60 when complex hydrodynamic phenomena (such as breaking waves) are present.

Previous experimental and numerical findings highlighted the uncertainties surrounding the influence of wall inclination on the breaking wave pressure. Furthermore, relationships between the impact pressure and wall inclination on an elevated structure located above the still water level (SWL) remain unknown. Based on this knowledge gap, the objective of this paper is to ascertain the influence of wall inclination and the structure's elevation to the wave pressures produced by a breaking wave. To achieve the objective of this study, the SPH program DualSPHysics was used to model an elevated structure with its front wall inclined at positive 15°, 0° (vertical), and negative 15° exposed to a breaking wave. Four different levels of building elevation were considered: (1) on-grade (bottom of structure in contact with the ground), (2) semi-submerged (bottom of structure above ground but below the SWL), (3) still water level (bottom of structure at SWL with no air gap), and (4) fully elevated (bottom of structure located above SWL with an air gap). The SPH formulations deployed in DualSPHysics pertinent to single and multiphase flows are described in Section 2. To ensure that wave-structure interactions can be accurately simulated, a validation study against experimental results in the literature is presented in Section 3. Bathymetric parameters, wave characteristics, structural geometries, and pressure measurements used to achieve the aim of the study are explained in Section 4. Findings and analyses are described in Section 5 and lessons learned from the experiment are summarized and concluded in Section 6.

2. SPH formulation

2.1. SPH formulation for single-phase fluid simulations

Smoothed-particle hydrodynamics is a Lagrangian meshless method which discretizes a fluid continuum into individual fluid particles. Particle trajectories are calculated based on the discretized Navier-Stokes equations using the fluid properties provided in each particle. Measured properties such as pressure, density, and velocity at a specific location are computed based on the influence of neighboring particles at a distance determined by the smoothing length (h) for either 2D (circular) or 3D (spherical) domains. The influence of each particle inside the smoothing length is weighted using a kernel function (W) so that the value of a variable (F) at position r can be approximated based on its neighboring particles at r':

$$F(\boldsymbol{r}) = \int F(\boldsymbol{r}')W(\boldsymbol{r}-\boldsymbol{r}', h)d\boldsymbol{r}' \tag{1}$$

or using the discrete form:

$$F(\boldsymbol{r}_a) \approx \sum_b F(\boldsymbol{r}_b)\frac{m_b}{\rho_b}W(\boldsymbol{r}_a-\boldsymbol{r}_b, h) \tag{2}$$

where a and b denote individual particles, and m_b and ρ_b denote particle b's mass and density, respectively. The kernel function W is defined using the normalized distance between particles q which is equal to $q = r/h$ following the Quintic formulation after Wendland (1995):

$$W(q) = \alpha_d\left(1-\frac{q}{2}\right)^4(2q+1)\ for\ 0 \le q \le 2 \tag{3}$$

where $\alpha_d = 7/4\pi h^2$ for 2D domains applied in the current study. Based on the formulae shown in Eqs. (2) and (3), the momentum equation applied to particle a based on the neighboring particles b can then be estimated using Monaghan (1992):

$$\frac{d\boldsymbol{v}_a}{dt} = -\sum_b m_b\left(\frac{P_b+P_a}{\rho_b\rho_a}+\Pi_{ab}\right)\nabla_a W_{ab} + \boldsymbol{g} \tag{4}$$

where g denotes the gravitational acceleration, P is the pressure evaluated at particle a or b, W_{ab} is the kernel function between particles a and b, and the artificial viscosity term Π is given by:

$$\Pi_{ab} = \begin{cases} \dfrac{-\alpha\,\overline{c_{ab}}\mu_{ab}}{\overline{\rho_{ab}}}\ for\ \boldsymbol{v}_{ab}.\boldsymbol{r}_{ab} < 0 \\ 0\ for\ \boldsymbol{v}_{ab}.\boldsymbol{r}_{ab} \ge 0 \end{cases} \tag{5}$$

$$\overline{\rho_{ab}} = 0.5\ (\rho_a+\rho_b) \tag{6}$$

$$\boldsymbol{r}_{ab} = \boldsymbol{r}_a - \boldsymbol{r}_b \tag{7}$$

$$\boldsymbol{v}_{ab} = \boldsymbol{v}_a - \boldsymbol{v}_b \tag{8}$$

$$\mu_{ab} = \frac{h\boldsymbol{v}_{ab}.\ \boldsymbol{r}_{ab}}{(r_{ab}^2+\eta^2)} \tag{9}$$

$$\overline{c_{ab}} = 0.5\ (c_a+c_b) \tag{10}$$

Where v denotes the particle's velocity, c denotes the speed of sound, $\boldsymbol{r}_{ab}$ denotes the distance between particles a and b, and α is the dissipation coefficient in the artificial viscosity term and is set to 0.01 based on a sensitivity study (see Section 3) and recommendations from the literature (Reis et al., 2022; Sato et al., 2021; Altomare et al., 2015, 2014). Furthermore, η^2 should be set to $0.01h^2$ to avoid numerical divergence when the distance between particles tends to zero (Crespo et al., 2015). In SPH, the mass remains constant for each particle with only the pressure density fluctuating following Eq. (11) (Fourtakas et al., 2020, 2019):

$$\frac{d\rho_a}{dt} = \sum_b m_b\boldsymbol{v}_{ab}.\nabla_a W_{ab} + \delta_\varphi hc_s\sum_b 2\ \left(\rho_{ab}^T-\rho_{ab}^H\right)\frac{\boldsymbol{r}_{ab}}{r_{ab}^2}.\nabla_a W_{ab}\frac{m_b}{\rho_b} \tag{11}$$

$$\rho_{ab}^H = \rho_0\left(\sqrt[\gamma]{\frac{\gamma(\rho_0 g z_{ab}+1)}{c_s^2\rho_0}}-1\right) \tag{12}$$

Here, δ_φ is a diffusion coefficient taken to be 0.1 as recommended by Sato et al. (2021), γ denotes the polytrophic constant, z_{ab} is the height difference between particle a and b, and c_s denotes the reference fluid speed of sound. To maintain a reasonable simulation time step, an artificially lowered speed of sound can be deployed with a value of at least ten times faster than the maximum fluid velocity as suggested by Monaghan et al. (1999). In the current study, a value equal to twenty times the maximum fluid velocity was adopted for water particles. For air particles, however, the allowable value of speed of sound depends on the Mach number, water phase density variations, and the maximum instantaneous velocity of the water phase on each time step (Khayyer et al., 2016). This allowable speed of sound value, furthermore, will expand as the simulation proceeds. To avoid error related to air density variation, the physical value of 343 m/s was taken. An equation of state is subsequently used to determinate the fluid pressure following the relationship proposed by Monaghan (1994) and Batchelor (1967):

$$P = C_B\left[\left(\frac{\rho}{\rho_0}\right)^\gamma - 1\right] \tag{13}$$

where C_B is a parameter that represents the compressibility of the fluid and can be calculated using:

$$C_B = c_s^2\frac{\rho_0}{\gamma} \tag{14}$$

where ρ_0 denotes the reference fluid density (997 kg/m^3 in our case for fresh water at room temperature) and γ is the polytrophic constant with 7 selected for the current study (Altomare et al., 2015). The pressure-density relationship shown in Eq. (13) follows the relationship described by Tait's equation where a small oscillation in density will generate a large variation in pressure.

To ensure the stability of the particles in SPH, especially in highly turbulent flows such as sloshing where the particles cannot maintain a uniform distribution, a shifting algorithm is needed. This algorithm functions as a way to move particles from densely populated regions toward areas with fewer particles as dictated by Fick's Law to avoid any voids (area with no particles) forming inside the domain. The full shifting distance ($\delta\boldsymbol{r}_s$) is formulated based on the particle concentration C and can be written as (Domínguez et al., 2022):

$$\delta\boldsymbol{r}_s = S\nabla C \tag{15}$$

$$S = Ah\|\ \boldsymbol{v}\ \|_a dt \tag{16}$$

where A denotes the shifting coefficient and is within a range between -1 to -6, v is the fluid velocity, and dt denotes the current time step. A shifting coefficient of -2 is taken in the current study.

2.2. SPH formulation for multiphase fluid simulations

In cases where there are two fluids interacting with each other, such as air trapped by moving water inside a chamber or within a breaking wave, the SPH model in DualSPHysics uses a modified version of Tait's equation of state (Eq. (13)) to calculate the multiphase fluid pressure (P_{mp}) as proposed by Mokos et al. (2017):

$$P_{mp} = \frac{c_s^2\rho_0}{\gamma}\left[\left(\frac{\rho}{\rho_0}\right)^\gamma - 1\right] + X - \left(1.5g\left(\frac{\rho_w}{\rho_a}\right)L\right)\rho^2 \tag{17}$$

where ρ_w and ρ_a denote the initial water and air densities, respectively, X is the constant background pressure and is taken as 0 (Mokos et al., 2017; Sato et al., 2021), c_s is the speed of sound, and L is the characteristics length scale which is equal to the water depth in current study. For the gas phase, however, an additional cohesion force is needed within the momentum equation (Nugent and Posch, 2000):

$$\frac{d\boldsymbol{v}_a}{dt} = -\sum_b m_b\left(\frac{p_a+p_b}{\rho_a\rho_b}+\Pi_{ab}\right).\nabla_a W_{ab} - 2\left(1.5g\left(\frac{\rho_w}{\rho_a}\right)L\right)\rho_a^2\sum_b\frac{m_b}{\rho_b}\nabla_a W_{ab} \tag{18}$$

Finally, to avoid void development (especially in highly violent flows), a modified version of Eq. (19) is used in 2D multiphase simulations (Lind et al., 2012; Monaghan, 2005; Violeau and Rogers, 2016) to define the full shifting distance, $\delta\boldsymbol{r}_s$:

$$\delta \boldsymbol{r}_s = S\left(\frac{\partial C_a}{\partial s}\boldsymbol{s}_a + \alpha_n\left(\frac{\partial C_a}{\partial n} - \beta_n\right)\boldsymbol{n}_a\right) \tag{19}$$

$$\boldsymbol{n}_a = -\frac{\nabla C_a}{\| \nabla C_a \|} \tag{20}$$

$$\boldsymbol{s}_a = \boldsymbol{R}\boldsymbol{n}_a \tag{21}$$

Here, $\boldsymbol{s}_a$ and $\boldsymbol{n}_a$ are the tangent and normal vectors to the free surface for a given particle a and $\boldsymbol{R}$ denotes the rotation matrix; β_n is the reference concentration gradient; α_n denotes the diffusion limit in the direction normal to the free surface and is set to 0 in current study (Lind et al., 2012). The particle concentration C_a and gradient of particle concentration ∇C_a can be calculated via:

$$C_a = \sum_b \frac{m_b}{\rho_b} W_{ab} \tag{22}$$

$$\nabla C_a = \sum_b (C_b - C_a)\frac{m_b}{\rho_b}\nabla W_{ab} \tag{23}$$

It can be noted that the modification of Eq. (19) is also considered in the single-phase model on free surface and its vicinity area. Furthermore, the latest development of shifting equation called Optimized Particle Shifting (OPS) is absent in current explorations (Khayyer et al., 2017).

2.3. Wave generation

There are two common wave generation methods in SPH, moving boundary and internal generation. In the latter method, the Boussinesq equations are used to derive a momentum source which is then applied into the weakly-compressible SPH model using Lagrangian Navier-Stokes equations. Moving boundary, however, is the most popular method used to generate wave trains in SPH and was used in this study. This method imitates the movement of a piston-type wave maker commonly used by wave testing facilities around the world in a numerical wave flume. A moving boundary is added to one side of the numerical flume and acts as a wave generator and wave absorber. Both first- and second-order waves can be generated by DualSPHysics, with the former being fully described in (Altomare et al., 2017 and Domínguez et al., 2019a) and can be applied for both regular and irregular waves. In this case, the second order wave equation was utilized, where the piston displacement equals:

$$e(t) = \frac{H}{2m}\sin(\omega t + \delta) + \left[\left(\frac{H^2}{32d}\right)\left(\frac{3\cosh(kd)}{(\sinh(kd))^3} - \frac{2}{m}\right)\right]\sin(2\omega t + 2\delta) \tag{24}$$

where m is defined as follows:

$$m = \frac{2(\sinh(kd))^2}{\sinh(kd)\cosh(kd) + (kd)} \tag{25}$$

Second-order waves are limited to $HL^2/d^3 < 8\pi/3$, where H denotes the wave height, L denotes the wavelength, and d is the water depth. Furthermore, $\omega = 2\pi/T$ denotes the angular frequency calculated using period (T), $k = 2\pi/L$ is the wave number, and δ denotes the initial phase. The piston displacement is then computed based on the wave height, wavelength, and water depth. To generate only a single wave, the piston movement is then limited to a single wave period before the piston moves back to the original position and stops.

3. Numerical modeling parameters and validation

Both single-phase (water particles only) and multiphase (air and water particles) scenarios were employed in SPH to study their discrepancies when simulating breaking wave phenomena. As discussed in Section 2, several parameters must be selected by the user of SPH to perform the simulations. This section first presents the experimental study used for the numerical validation, and then evaluates the selection of key numerical parameters such as boundary condition, inter-particle distance, and artificial viscosity.

3.1. Experimental study for validation

A breaking wave impact on an elevated inclined wall was compared against a physical model experiment described in (Müller and Whittaker, 1993). The validation was done using a 14 m long and 1.5 m deep 2D numerical wave flume modeled after Müller and Whittaker (1993) as shown in Fig. 1. The wave was generated using a piston-type wavemaker located 0.5 m from the upstream end of the flume and simulated using moving boundary particles. The still water level is 1 m deep at the piston and reduces in depth along a 1:10 sloping beach to 0.115 m deep at the structure's location on the elevated berm. The flat berm extends 0.935 m to the downstream end of the flume. A fully closed Oscillating Water Column (OWC) chamber was placed 13.153 m from the wave maker to reflect the experiment. The structure's semi-submerged front wall (inclined 32.7°) is 0.3 m high and 0.1 m thick with its bottom located 0.045 m below the still water level (0.07 m above the channel floor).

3.2. Boundary conditions

Both Dynamic boundary conditions (DBC) and modified dynamic boundary condition (mDBC) were adopted in the current study where particles constituting a solid boundary satisfy the same equations of continuity and state as the fluid particles but remain in place or move in accordance with a predetermined function. These types of boundaries are relatively easy to set up and robust for numerical simulations with complex geometries (Altomare et al., 2015). In DBC, however, an unphysical gap may form between the boundary of solid and fluid particles, thus decreasing the pressure measurement accuracy. In mDBC, this gap is eliminated by implementing ghost nodes to extrapolate the position of the boundary particles, allowing pressures to be measured closer to a solid surface (English et al., 2022).

The DBC vs mDBC comparison of the single-phase simulation is shown in Fig. 2a and b. A slight gap can be seen between the water particles and the structure for the DBC simulation (Fig. 2a) that is not present for mDBC (Fig. 2b). Fig. 2c shows the pressure maxima time series taken on the front wall of the structure for both DBC and mDBC models. The mDBC simulation shows a clear impact pressure that is not present for the DBC case, which also shows increased noise often associated with DBC (Altomare et al., 2021). Based on this comparison, only mDBC were considered for single-phase simulations. Unfortunately, since DualSPHysics limits mDBC to only single-phase problems, the commonly used DBC was implemented for multiphase models.

3.3. Numerical parameters: inter-particle distance (dp) and artificial viscosity (α)

To get an accurate representation of wave simulation, an inter-particle distance sensitivity test was done prior to the actual simulation with H/dp ranging from 33 to 50 as suggested by prior studies (Altomare et al., 2023; Reis et al., 2023). To induce wave breaking on the elevated wall, a second order wave with wave height (H) 0.1 m and wave period (T) of 1.49 s was generated using a moving piston (Eq. (26)). The piston stroke was timed to only generate a single wave before returning to its original position and ceasing movement.

Table 1 summarizes the simulation settings for the dp sensitivity test, including the total number of particles and the simulation time for each inter-particle distance. Fig. 3a compares the pressure maxima measured at the front wall of the structure for the single and multiphase simulations alongside the experimental observation from Müller and Whittaker (1993). As expected, SPH pressure measurements approach the experimental result with decreasing dp. An inter-particle distance of

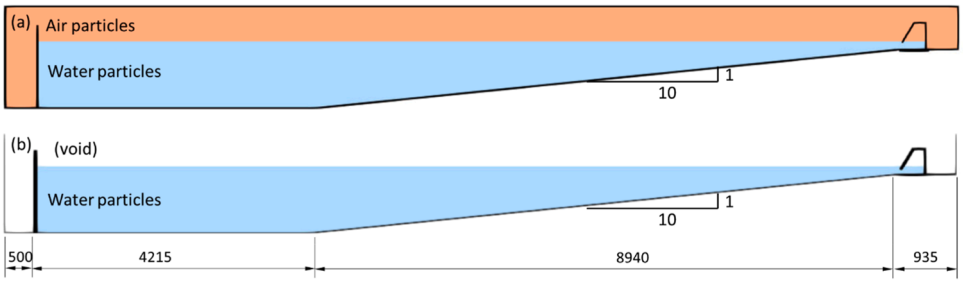

Fig. 1. Numerical setup after Müller and Whittaker (1993) for (a) multiphase and (b) single-phase simulations. All dimensions in mm.

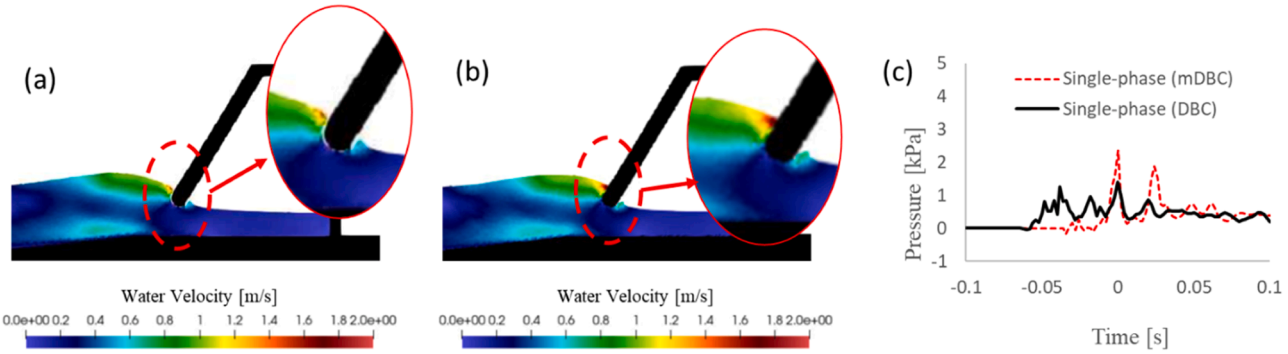

Fig. 2. Flow visualization of the single-phase DualSPHysics simulation using (a) DBC and (b) mDBC type boundary conditions, and (c) the maximum pressure measured at the front wall of the structure.

Table 1
Simulation conditions for inter-particle distance (*dp*) sensitivity study.

Simulation type	Boundary condition	*dp* [m]	Total # of particles	Total simulation time
Single-phase	mDBC	0.003	1042,883	60 min
		0.0025	1495,179	1 h 30 min
		0.002	2330,902	2 h 20 min
Multiphase	DBC	0.003	1903,686	38 h 24 min
		0.0025	2737,759	69 h 5 min
		0.002	4271,646	139 h 3 min

0.002 m resulted in the best performance for both the single-phase and multiphase simulations. Considering that the difference in results is small for $dp = 0.002$ m and 0.0025 m for the multiphase simulations, and the high computational time of 139 h (Table 1) for $dp = 0.002$ m, a value of $dp = 0.0025$ m was adopted for multiphase scenarios. For single phase simulations, however, the inter-particle distance adopted was 0.002 m.

Recent findings suggest the artificial viscosity coefficient (α) to be important when modeling breaking waves generated in SPH. Reis et al. (2022) and Sato et al. (2021) suggested an α value of 0.01, while Altomare et al. (2023) suggested 0.028. To get a suitable value of α, a sensitivity study was done across a range between 0.005 and 0.04 as shown in Fig. 3b using the selected *dp* values (0.002 m and 0.0025 m for the single-phase and multiphase, respectively). It is seen that the lowest value of $\alpha = 0.005$ exhibits the highest pressure. However, flow visualization showed that the wave broke much earlier than the structure and was not consistent with the experiment where a breaking wave was observed to impinge the inclined front wall of the structure (Müller and Whittaker, 1993). Conversely, α values ≥ 0.02 produced a non-breaking wave and was also inconsistent with experimental results. A value of α equal to 0.01 produced an impact pressure with the wave breaking on the structure as expected and was adopted for the current study for both the single-phase and multiphase simulations.

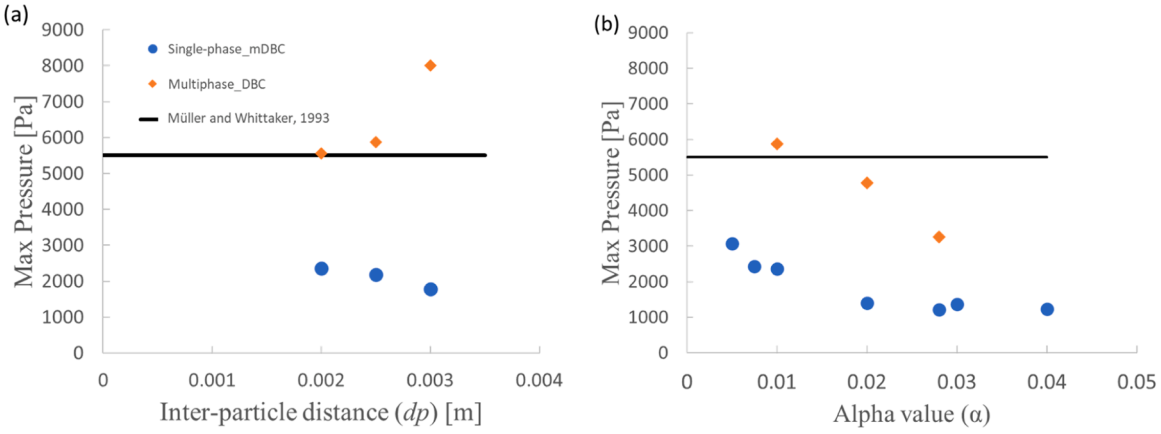

Fig. 3. (a) Inter-particle distance (*dp*) and (b) artificial velocity (α) sensitivity study for single-phase, multiphase, and experiment after Müller and Whittaker (1993).

3.4. Validation results

Using the *dp* and α values selected as discussed above, Fig. 4 shows the flow visualization for both multiphase (Fig. 4a) and single-phase (Fig. 4b) simulations. Here, t^* indicates the non-dimensional time of the instantaneous visualization (t_v) relative to the time of impact (t_i) and normalized by wave period (T), or $t^* = (t_v - t_i)/T$. The light blue color in Fig. 4a indicates the air particles, while the empty color above the water particles in Fig. 4b indicates a void. The water particle color here represents the water velocity. It can be seen from Fig. 4a that the wave breaks just before the structure with an air pocket trapped between the impinging water and the front wall of the structure. It can be inferred that a plunging breaking wave was produced via the multiphase model whereas the single-phase simulation (Fig. 4b) shows a breaking wave resembling a spilling breaker (Cooker and Peregrine, 1992). This resulted in a lower impact pressure when compared to both the experiment and multiphase approach.

Since different types of breaking waves were observed for the single and multiphase simulations (Figs. 4a vs 4b), additional simulations were performed without the OWC structure as shown in Fig. 5. These beach-only studies indicate that wave breaking occurred 0.097 m behind the location of the original structure, where the dashed red line shown in Fig. 5 indicates the location of the breaking wave in the multiphase simulation when compared to the single-phase results. This difference in breaking behavior is similar to observations by Lind et al. (2017) who suggested that air particles modify the local free-surface profile of the breaking wave. To get a better comparison between the single and multiphase models, the single-phase structure was moved 0.097 m away from its original location such that a plunging breaker will impact the wall (Fig. 4c). Another discrepancy in Fig. 5 relates to the difference in "bumpiness" of the free-surface profile between the multiphase and the single-phase models. This may be caused by the interaction between air (light blue) and water particles.

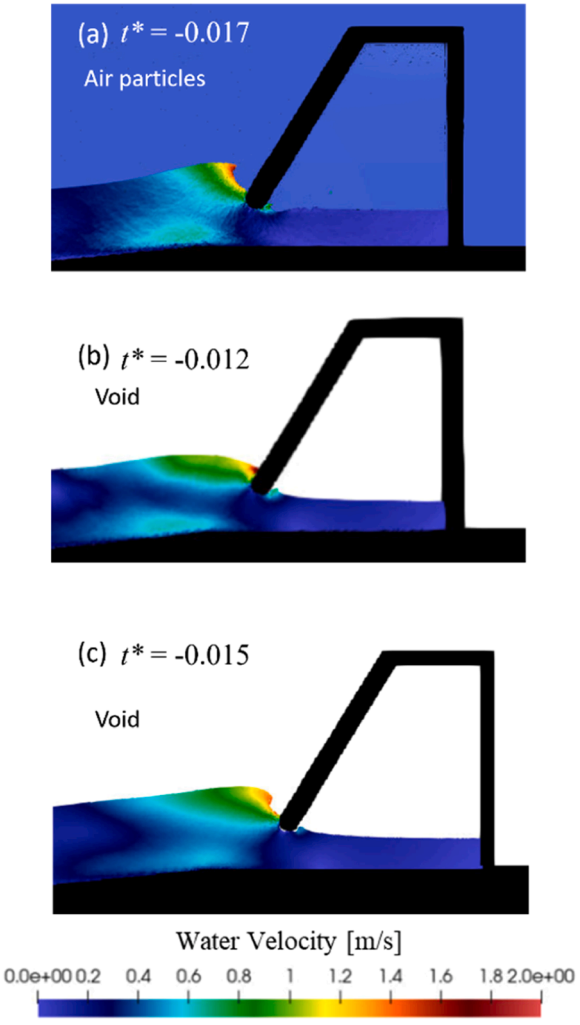

Fig. 4. Flow visualization of breaking wave simulated hitting the inclined wall using (a) multiphase SPH, (b) single phase SPH at original wall position, and (c) single phase SPH with wall shifted by 0.097 m away from the piston.

Fig. 6 shows the pressure time-series corresponding to the maximum breaking wave pressure for multiphase SPH (Fig. 4a), single-phase SPH at original position (spilling breaker in Fig. 4b), single-phase SPH at moved position (plunging breaker in Fig. 4c), and experimental results per Müller and Whittaker (1993). The pressure is compared only for the location where the highest pressure was measured. It can be seen that both multiphase and single-phase with moved structure reached a similar impact pressure of 5.9 kPa, or an overestimation of about 7 % to the experimental data, making the results conservative. The multiphase simulation, however, produced a pressure rise time (the time needed from zero pressure to peak pressure) that is more consistent with the experiment than both single-phase models. Furthermore, the single-phase spilling breaker underestimated the impact pressure by 56 %. It was also observed that the multiphase pressure has wide fluctuations between positive and negative after the initial impact. This fluctuation is caused by acoustic pressure noise associated with weakly compressible SPH methods as explained in detail by Cooker (2002) and Meringolo et al. (2017). Sun et al. (2023) proposed an acoustic damping term to be included in SPH simulation to reduce such noise. This term, however, has yet to be available for multiphase DualSPHysics. Nevertheless, the initial impact load (the main focus of the study) shows good agreement with the experiment. Fig. 7 shows the pressure field at the moment of impact for both multiphase simulation (a), and single-phase simulation (b). A high local pressure, indicated by red color, can be seen at the tip of the breaking wave in both cases. For the multiphase simulation (Fig. 7(a)), the red dashed line indicates the free water surface between the water particles and the air particles.

In addition to the pressure maxima experienced by the front wall, the pressure peaks measured at various vertical positions of the inclined wall are compared with the 99.99 % probability envelope proposed in Müller and Whittaker (1993) based on their experiments. The inside of that envelope is shaded in Fig. 8, where the possibility of pressures going outside of envelope is only about 1 in 10,000 or 0.01 %. The comparison of the envelope to the SPH simulations show that both single and multiphase results do not exceed the 99.99 % probability envelope with the exception of the pressure sensors located above 0.075 m where the probability line goes to zero. These numerical pressure measurement points were generated due to water splashing upward after the initial impacts. In a 2D numerical simulation, the water only has one plane to travel and will hit the pressure sensors' location. In a physical model, or real live situation, this water splash will likely go everywhere thus less likely to give any meaningful pressure measurement at predetermined pressure location. Nevertheless, the pressures measured above the probability line were much smaller when compared to the impact pressure and thus can be ignored.

Based on these results examining pressure and wave impact visualization, it can be concluded that both multiphase and single-phase approaches in DualSPHysics are able to simulate a breaking wave impact with good similarities to experimental observations, albeit with slight modification for single-phase approach. Furthermore, waves in the multiphase simulation better represent the governing physics relevant to breaking wave phenomena (Sun et al., 2019; Lind et al., 2017). As such, only the multiphase approach was employed for the parametric study involving elevated structures.

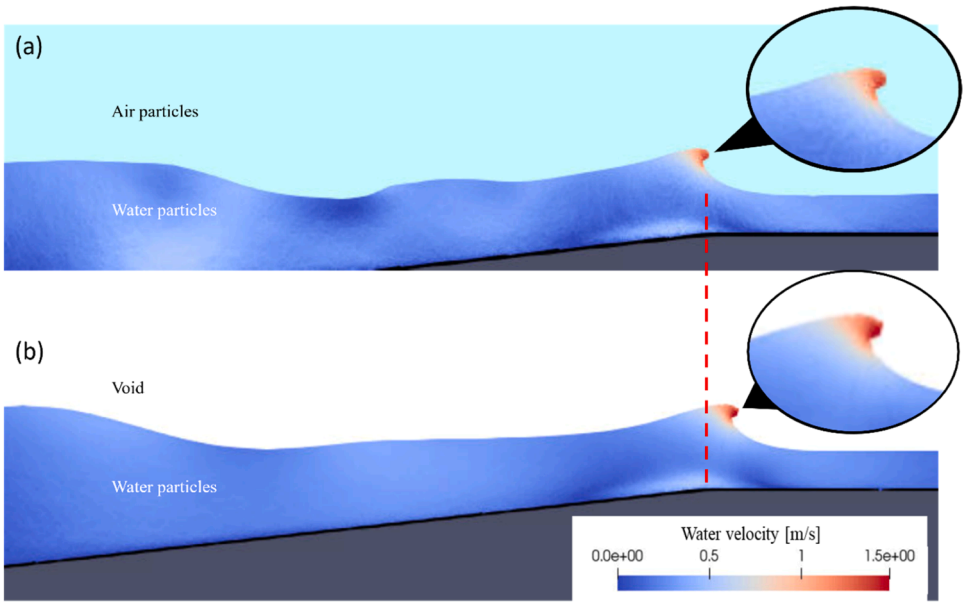

Fig. 5. Flow visualization of the numerical wave flume without the structure for (a) multiphase SPH simulation and (b) single-phase SPH simulation. The dashed red line indicates the location where the wave brakes in the multiphase simulation.

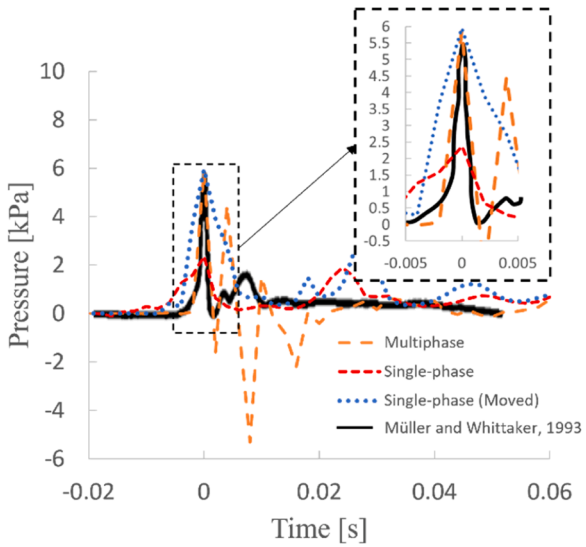

Fig. 6. Pressure time series comparison of multiphase simulation, single-phase simulation (spilling breaker), SPH simulation (Moved - plunging breaker), and experiment after Müller and Whittaker (1993).

4. Numerical setup and parameters of study

4.1. Bathymetric parameters

To understand the influence of wall inclination on breaking wave pressures exerted on an elevated coastal structure, a case study based on waves produced from Hurricane Sandy was used. Bathymetry corresponding to Monmouth Beach at 40°20′04″ N 73°58′28″ W on the east coast of New Jersey was selected as it experienced the largest inundation during Hurricane Sandy at 2.7 m (Wang et al., 2022). A 2D 260 m long and 20 m high numerical wave flume containing both water and air particles was constructed using multiphase SPH via DualSPHysics v5.0. A piston-type wave generator located 10 m away from the upstream end of the flume leads to a 100 m long flat seabed followed by a 1:15.6 slope leading to a 6.4 m high berm spanning 50 m to the downstream end (Fig. 9). The SWL exists 9.1 m above the deepest part of the flume (2.7 m above the berm) to reflect the maximum level of inundation observed during hurricane Sandy (Wang et al., 2022).

4.2. Wave characteristics

A single regular wave with wave height (H) equal to 3.8 m and wave period (T) equal to 8.3 s was selected to reflect the significant wave height and peak period estimated at the site (Wang et al., 2022; Lichtenwalner, 2023). This condition represents a breaking wave on the berm according to Le Méhauté's (2013) diagram as shown in Fig. 10. Due to the complexity of breaking wave phenomena, only multiphase SPH simulations were implemented. The intention was to generate a plunging breaker (similar to the validation study – see Fig. 4) where a curling crest envelops a pocket of air which may result in the highest pressure experienced by a wall (Cooker and Peregrine, 1992).

4.3. Structural configurations of study

To achieve the study's aims, three structural configurations were considered with different front wall inclinations: vertical (Fig. 11a), positive 15° inclined (Fig. 11b), and negative 15° inclined (Fig. 11c). These inclinations were chosen based on the study done by (Müller and Whittaker, 1993) which concluded that a positive wall inclination reduces the impact pressure, albeit with a different configuration. A 6 m high by 10 m long structure was selected based on (Park et al., 2017) which represent a typical two-story building in the United States of America. The structure was placed 219 m from the piston when measured at the SWL. This location was determined based on the location of the breaking wave during the preliminary multiphase SPH simulation of the flume without the structure.

In addition to the three wall inclinations, four different elevations were considered as demonstrated by Fig. 12. These include the structure touching the seabed or *on-grade* (Fig. 12a); the structure *semi-submerged* (negative air gap) with a 1.35 m opening below the structure allowing water passage (Fig. 12b); the structure located at the *still-water level* (Fig. 12c); and the structure *elevated* 1.35 m above the still-water level (positive air gap) or 4.05 m above the seabed (Fig. 12d). These parameters are further summarized in Table 2.

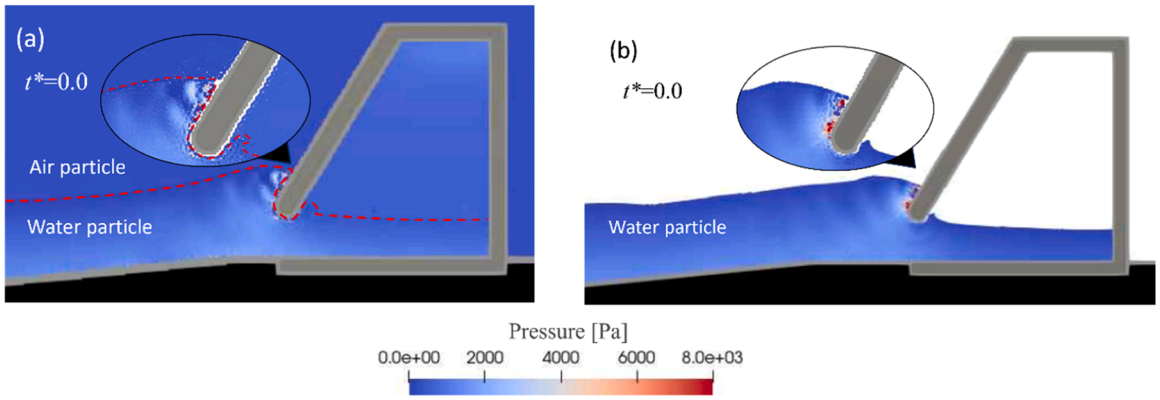

Fig. 7. Spatial distribution of pressure for (a) air and water particles in multiphase simulation and (b) water particles in single-phase simulation, at the moment of breaking wave impact. The red dashed line indicates the free water surface between the water particles and the air particles for multiphase simulation.

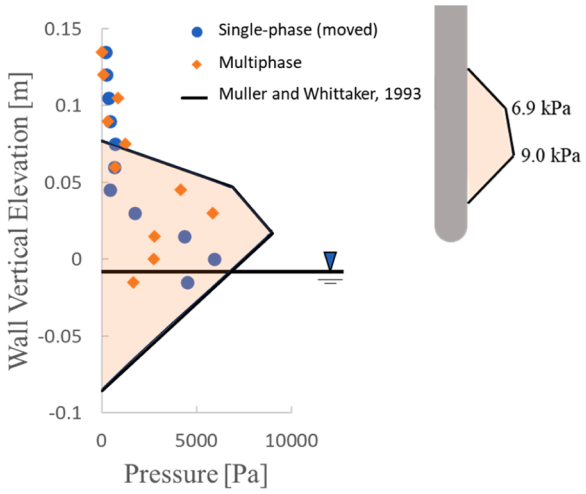

Fig. 8. Vertical distribution of pressure maxima measurements compared to the 99.99 % probability of the maximum pressure on a 32.7° inclined wall after Müller and Whittaker (1993) as shown in top corner, compared with single-phase and multiphase simulations.

4.4. Pressure measurements

Fig. 13 shows where the pressures were measured on the structure. To record the horizontal pressures, 61 numerical pressure sensors (00–60) were placed on the front wall of the structure between the bottom and top corners at every 0.1 m interval. Furthermore, an additional 11 numerical pressure sensors (61 - 71) were placed along the bottom of the structure at 1 m intervals to measure the vertical pressure (excluding the On-Grade configuration due to the bottom of the structure being fixed to the seabed). The use of dynamic boundary conditions requires that the pressure (p) be taken at twice the smoothing length (2 h) from the solid boundary (Crespo et al., 2015).

4.5. Simulation properties and computational hardware

A 250 m by 20 m 2D simulation domain was used with 2085,403 particles generated for both water and air. The inter-particle distance was 0.05 m which gave a wave height (H) to inter-particle distance ratio of 76, thus exceeding that suggested by (Reis et al., 2022). The simulations were run using an NVIDIA® A100 GPU belonging to Princeton University's research computing facility with each case taking approximately 23 h on average to simulate 45 s of physical time.

5. Simulation results and analysis

5.1. Breaking wave characteristics

Fig. 14 shows the breaking wave impacting the structure at various wall inclinations (given by the columns) and at various elevations (given by the rows). It can be seen that the plunging breaker propagating towards the structure exhibits the same profile for each case and breaks directly on the structure with a similar degree of "cleanliness" (Müller and Whittaker, 1993). Therefore, it can be inferred that any differences in pressure measured on the front wall will be mostly influenced by the structure's inclination and elevation.

Nevertheless, the structure's presence does have an influence on breaking wave formation as seen in Fig. 14b, with the wave breaking earlier (i.e., further away from the structure) for positively inclined surfaces. This behavior was due to shoaling of the propagating wave induced by runup upon the positively inclined walls. To confirm this phenomenon, an additional test shifted the positively inclined structure 1.4 m upstream (model OnG_Pos_Forward in Table 2). Flow visualization subsequently showed the same phenomenon occurring where the wave breaks before impacting the structure. These findings support the argument that the bottom of a positively sloped structure interacting with incoming waves encourages premature breaking. Furthermore, the air particles' color represents the air pressure. It can be seen in Fig. 14f, g, and i that a high air pressure region was developed between the structure and the impinging wave. For the impact pressure analysis, however, zero denotes the ambient air pressure.

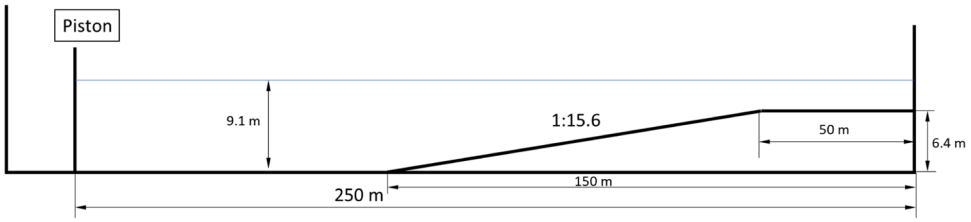

Fig. 9. 2D numerical wave flume depicting Monmouth Beach, New Jersey.

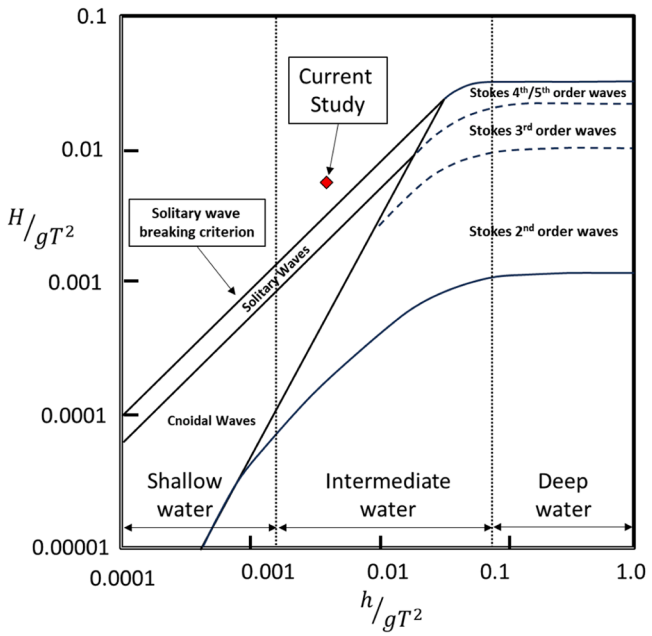

Fig. 10. Le Méhauté's Diagram showing the case study as the red diamond located above the breaking wave line for single regular wave (after Le Méhauté, 2013).

5.2. Influence of wall inclination to breaking wave impact loads

Fig. 15 shows the normalized horizontal pressure maxima measurement on the front wall of the structure at various inclinations for: (a) on-grade, (b) semi-submerged, (c) still-water level, and (d) fully elevated above the SWL. The normalized pressured (p_{nor}) is based on the incident wave height (H_{inc}) measured 1 m away from the front wall of the structure:

$$p_{nor} = \frac{p_{max}}{\rho g H_{inc}} \tag{26}$$

where p_{max} is the maximum measured pressure, ρ denotes the water density, and g denotes the gravitational acceleration. p_{nor} thus normalizes the maximum pressure against the potential energy of the incident wave given by the denominator. Note that Fig. 15 represents the peak normalized pressure independently measured at each location (which may not necessarily occur at the same time), thus giving a hypothetical worst-case scenario of the pressure envelope. A summary of the peak normalized pressures observed in Fig. 15 is shown in Fig. 16. Furthermore, it is important to confirm that Figs. 15 and 16 indeed depict impact pressures resulting from wave breaking. Impact pressures occur over an extremely short duration and can be organized into three

Table 2
Detailed parameters for parametric study with the name of each parameter combination.

Model Name	Elevation Description	Inclination Description	Elevation (m) Above berm To SWL (air gap)
OnG_Ver	**On**-Grade	**Ver**tical	(a) 0
OnG_Pos	**On**-Grade	**Pos**itive 15°	(b) −2.7
OnG_Neg	**On**-Grade	**Neg**ative 15°	
Semi_Ver	**Semi**-Submerged	**Ver**tical	(a) 1.35
Semi_Pos	**Semi**-Submerged	**Pos**itive 15°	(b) −1.35
Semi_Neg	**Semi**-Submerged	**Neg**ative 15°	
SWL_Ver	**S**till **W**ater **Lvl**	**Ver**tical	(a) 2.7
SWL_Pos	**S**till **W**ater **Lvl**	**Pos**itive 15°	(b) 0
SWL_Neg	**S**till **W**ater **Lvl**	**Neg**ative 15°	
Elev_Ver	**Elev**ated	**Ver**tical	(a) 4.05
Elev_Pos	**Elev**ated	**Pos**itive 15°	(b) 1.35
Elev_Neg	**Elev**ated	**Neg**ative 15°	
OnG_Pos_Forward (*)	**On**-Grade	**Pos**itive 15°	(a) 0 (b) −2.7

(*) The center bottom of all structures are positioned 219 m from the piston except OnG_Pos_Forward, which was placed 217.6 m away.

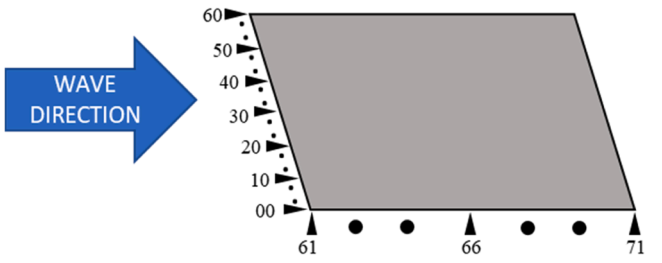

Fig. 13. Pressure sensors location at the front wall and the bottom of the structure.

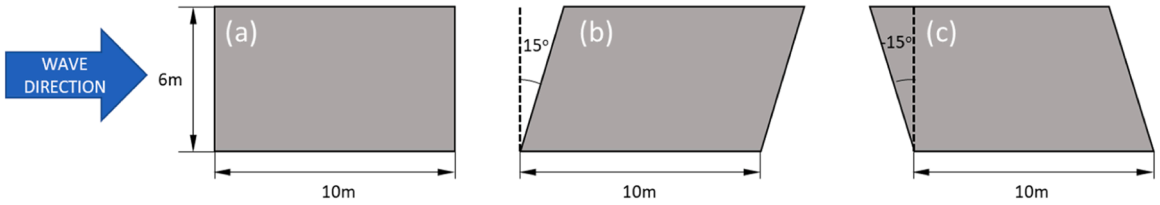

Fig. 11. Structural configurations considered: (a) vertical wall or 0° inclination, (b) positive 15° inclination, and (c) negative 15° inclination.

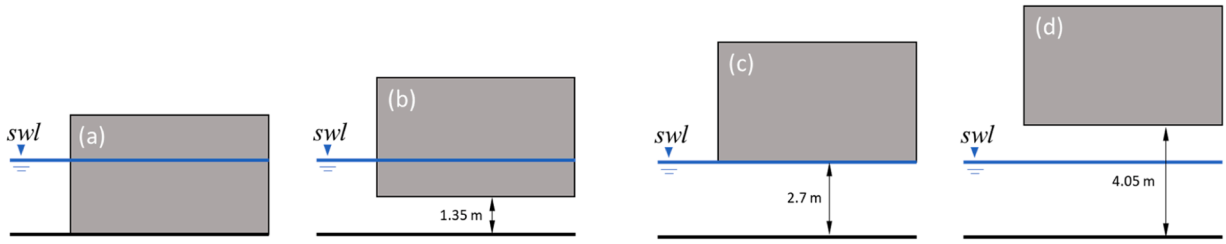

Fig. 12. Various structural elevations measured from the bottom of the elevated berm: (a) On-Grade or 0 m, (b) semi-submerged or 1.35 m from the flume's bottom, (c) Still-Water Level (SWL), and (d) elevated or 1.35 m above SWL.

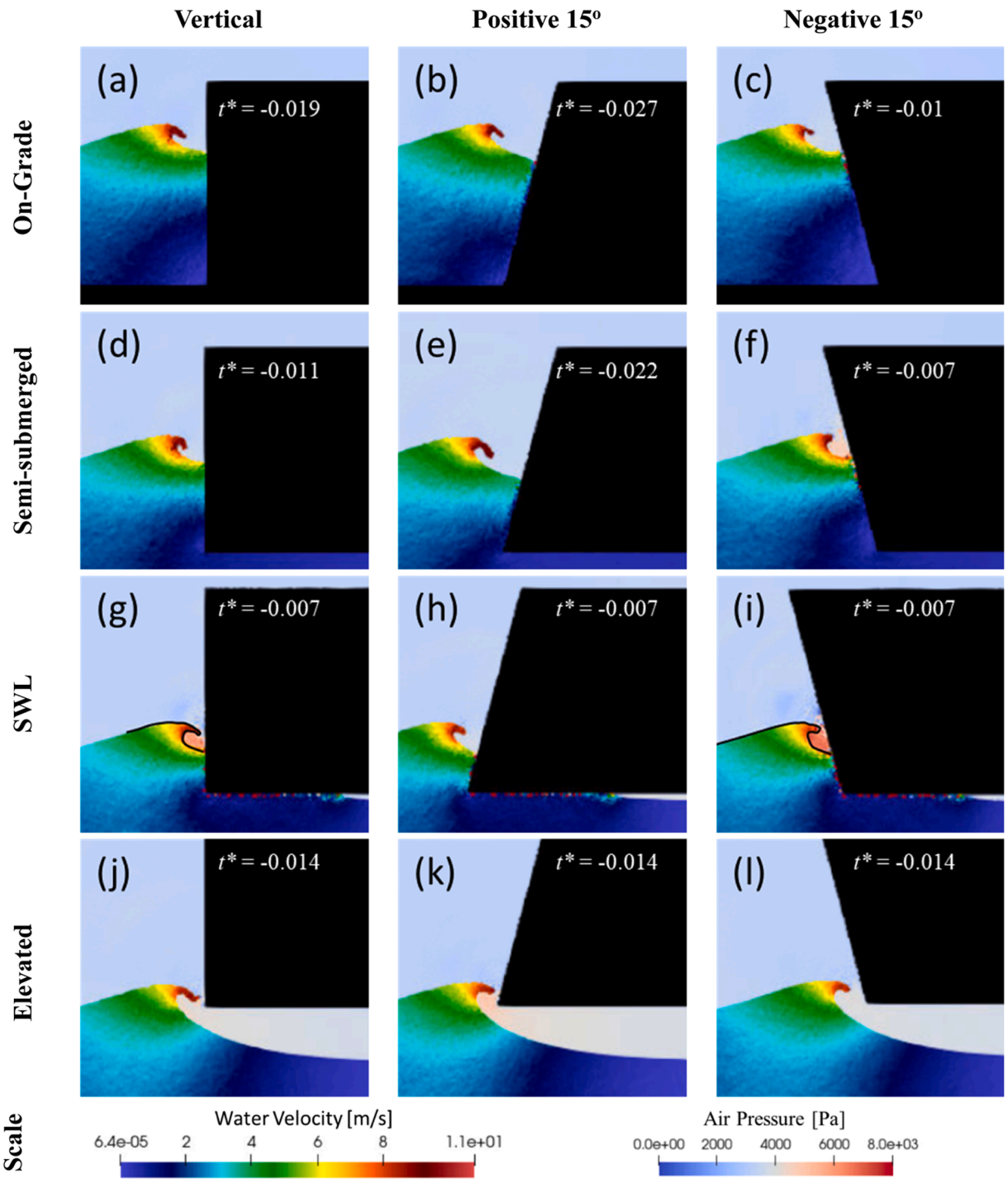

Fig. 14. Breaking wave profiles with color of water particles indicating the velocity magnitude. Flow visualizations depict (a) OnG_Ver, (b) OnG_Pos, (c) OnG_Neg, (d) Semi_Ver, (e) Semi_Pos, (f) Semi_Neg, (g) SWL_Ver, (h) SWL_Pos, (i) SWL_Neg, (j) Elev_Ver, (k) Elev_Pos, and (l) Elev_Neg. See Table 2 for more details.

different categories based on the rise time (t_r) relative to the incident wave period (T) (Pawitan et al., 2020; Oumeraci et al., 1993; Allsop et al., 1996). These categories consist of *severe impact* ($t_r < 0.01T$), *less severe impact* ($t_r < 0.1T$), and *near breaking impact* ($t_r \approx 0.2T$). Fig. 17 shows the normalized pressure time series for SWL_Ver at 1.1 m above the SWL as an example of the typical pressure experienced in these cases. The impact load rises from essentially zero to its peak value over t_r = 0.06 s, which is less than 0.01 times the wave period (T) of 8 s and thus can be characterized as *severe impact*.

For the On-Grade case (Fig. 15a), the highest pressure was recorded at negative 15° inclination with p_{nor} = 7.1 or about 1.5 times the pressure measured at the vertical wall. Contrarily, the positive 15° inclination showed a 22 % reduction in maximum pressure when compared against the vertical wall. This reduction in pressure is shown to occur due to premature wave breaking induced by the positive slope. A further reduction can be observed when the structure was shifted forward by 1.4 m as indicated by the special case. However, this result cannot be fairly compared with the vertical wall because the position of the structure changed. For the semi-submerged structure (Fig. 15b), the negative 15° inclination showed the highest impact maxima at p_{nor} = 6.5. Maximum pressures on the vertical and positively inclined wall followed at p_{nor} = 6.0 and 4.8, respectively. This inverse relationship

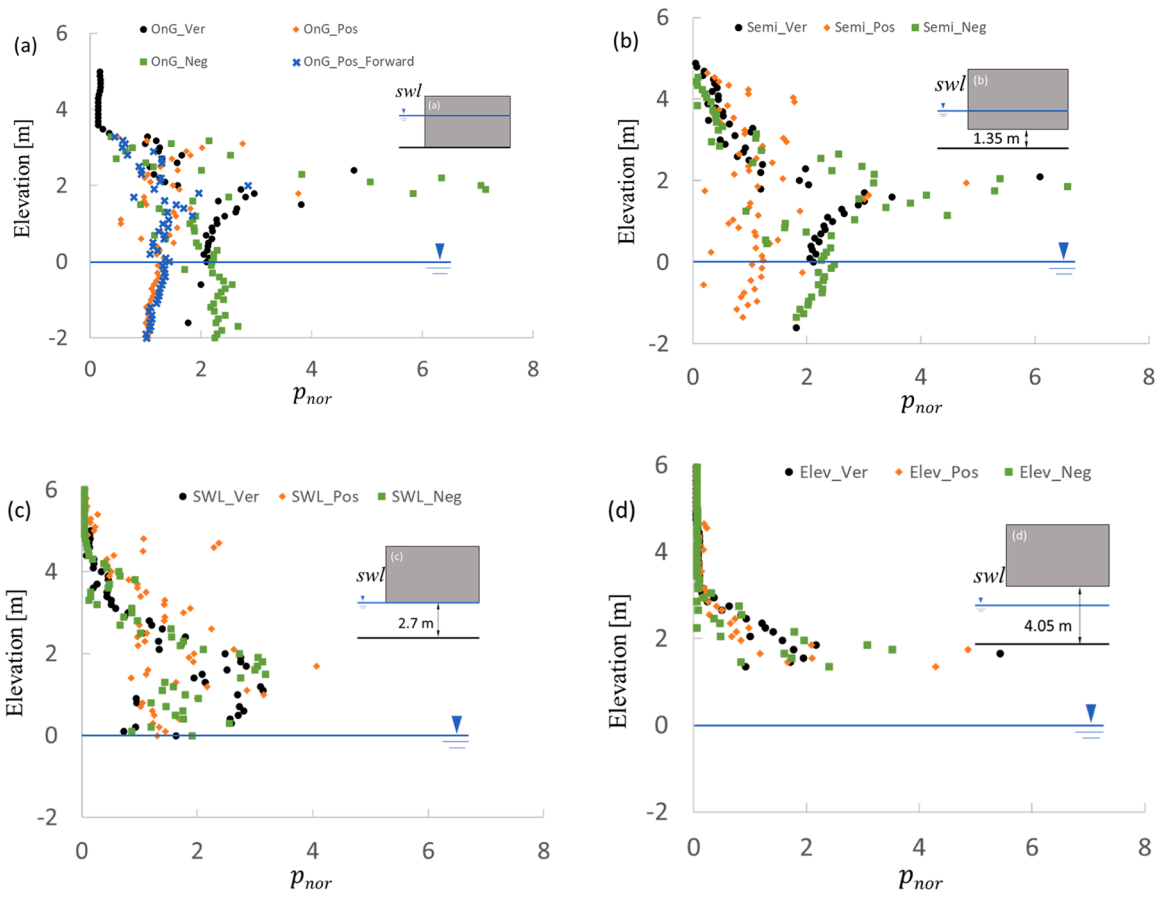

Fig. 15. Normalized peak pressure maxima measurement at various front wall inclinations for (a) On-Grade cases, (b) Semi-submerged cases, (c) Still-Water Level (SWL) cases, and (d) Elevated cases. Zero on y-axis indicates the SWL.

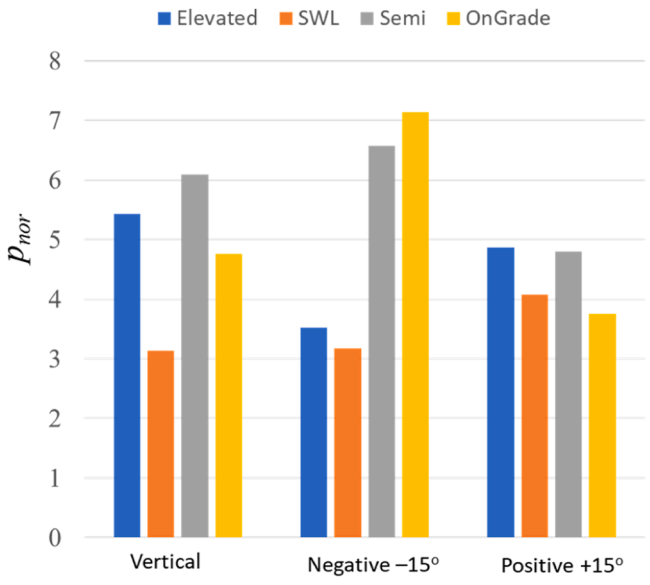

Fig. 16. Summary of Fig. 15 representing the peak normalized pressures for each case.

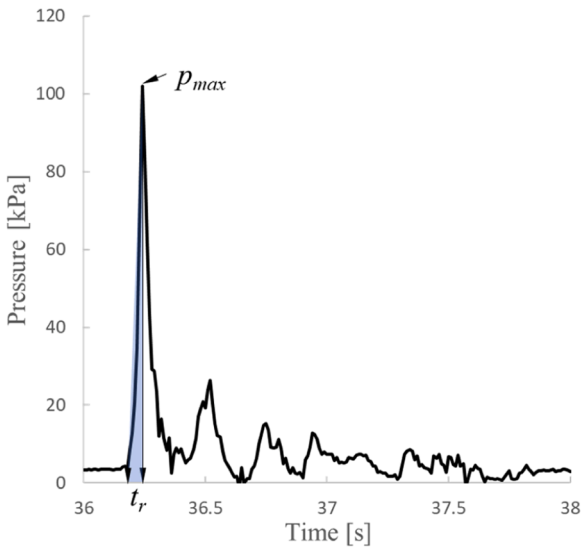

Fig. 17. Normalized pressure time series for SWL_Ver case, measured on the front wall at 1.1 m above the SWL.

between peak pressure and angle of inclination is clearly seen in Fig. 16. However, the differences in maximum pressure between vertical and inclined walls is less when compared to the On-Grade scenario.

The still-water level (SWL) elevation is shown in Fig. 15c. The highest pressure is measured at positive 15° inclination with $p_{nor} = 4.0$ occurring at 1.7 m above the SWL. Interestingly, both vertical and negative 15° inclinations have very similar results with the pressure peak of $p_{nor} = 3$ occuring 1 to 2 m above the still water level. Fig. 16 shows that the angle of inclination does not have a great effect on the peak pressure exerted by breaking waves on the front wall of a structure elevated to the SWL. The pressure experienced by the front wall when

the structure is elevated above the still-water level is shown in Fig. 15d. Interestingly, the vertical wall exhibits the highest breaking wave pressure of $p_{nor} = 5.4$. The positive 15° inclination showed the second highest pressure measurement of $p_{nor} = 4.8$. In contrast to the other elevations, the negative 15° inclination showed a significant 36 % reduction in peak pressure when compared to the vertical case.

As seen in Figs. 15 and 16, the SWL and elevated cases have the smallest pressures for surfaces inclined at negative 15°. Yet, the on-grade and semi-submerged cases exhibit the largest pressures at this inclination. To understand this trend, it is important to explain a phenomenon called "flip-though" which occurs when the water surface rises and shoots upward as it is being squeezed by the impinging breaker against a wall with minimal air entrainment (Cooker and Peregrine, 1992). Flip-through typically results in high impact pressures and is more apparent when the impact occurs above the SWL as further explained by (Bullock et al., 2007). This phenomenon can be observed in all cases, with the exception of the negative 15° case of the elevated structure (Elev_Neg) as demonstrated in Fig. 18c. Here, the evolution of the free surface is sketched via three timestamps: just before touching the structure (dotted line), as the wave hits the structure (dashed line), and after the wave passes the front wall of the structure (solid line). For comparison, other cases for the same structure elevation are also shown. The vertical and positive 15° configurations (Fig. 18a and b) show the propagating wave contacting the lower corner before the crest has collapsed thus shooting water upward in the direction of the arrows. For the negative 15° inclination, however, the crest is forced downward with minimal flip-through occurrence. This configuration resulted in the lowest peak pressure when compared with the vertical and positive inclinations.

5.3. Influence of structure elevation on breaking wave impact loads

In addition to assessing the influence of inclination at a constant structural elevation, it is also important to see if the structure's position relative to the SWL will have an influence on the impact pressure for a given inclination. In addition to Fig. 16 which compares peak normalized pressures, Fig. 19 presents the distribution of p_{nor} on the wall (similar to Fig. 15 but reorganized in terms of structure elevation).

It can be observed from Figs. 16 and 19 that on average, when the structures are elevated to the SWL (zero air gap), the measurements consistently resulted in the lowest normalized pressure relative to other elevations. In contrast, semi-submerged cases (negative air gap) generally resulted in the highest pressure. The pressure maxima on fully elevated structures (positive air gap) and the structures founded on-grade are greatly influenced by how the plunging breaker interacts with the -front wall as partly shown in Fig. 18 (a, b, c) and described in subSection 5.2.

5.4. Horizontal and vertical force comparison

In a monolithic bottom standing coastal structure such as a breakwater, the importance of horizontal force often receives priority because any upward force experienced by the structure due to waves is countered by the weight of the structure. However, for structures like an elevated bridge or house inundated during a storm, the foundation must offer sufficient strength to anchor the structure in place. In such cases, it is necessary to characterize the influence of front wall inclination to the total vertical force experienced by the structure.

To calculate the total horizontal and vertical forces acting on the structures employed in this study, an average of two pressure sensor measurements was used to represent the pressure acting on the area between the probes. The total force per unit width acting normal to the front wall and bottom surface thus equals to the summation of the averaged forces as follows:

$$(\boldsymbol{F}_{tot})_{front} = \sum_{n=00}^{60} \left(\frac{p_{\max,n} + p_{\max,n+1}}{2} \right) l_{n(n+1)} \tag{27}$$

$$(\boldsymbol{F}_{tot})_{bot} = \sum_{n=61}^{71} \left(\frac{p_{\max,n} + p_{\max,n+1}}{2} \right) l_{n(n+1)} \tag{28}$$

where $p_{max,n}$ and $p_{max,n+1}$ represents the maximum pressure measured at location n and the one adjacent $(n + 1)$, respectively, as measured parallel to the wall (see Fig. 13). The variable $l_{n(n+1)}$ is the distance between $p_{max,n}$ and $p_{max,n+1}$. Here, only the pressure measurement on the front wall is considered for the $(F_{tot})_{front}$, and similarly, only the pressure measurement on the bottom of the structure considered for $(F_{tot})_{bot}$. Fig. 13 shows details about the pressure sensor location. Since both $(F_{tot})_{bot}$ and $(F_{tot})_{front}$ are oriented normal to the wall surface, the angle of wall inclination θ must be considered to calculate the horizontal and vertical force components (where $\theta = 0$ for the vertical wall). The horizontal force per unit width (F) is directly calculated from the pressure on the front wall as follows:

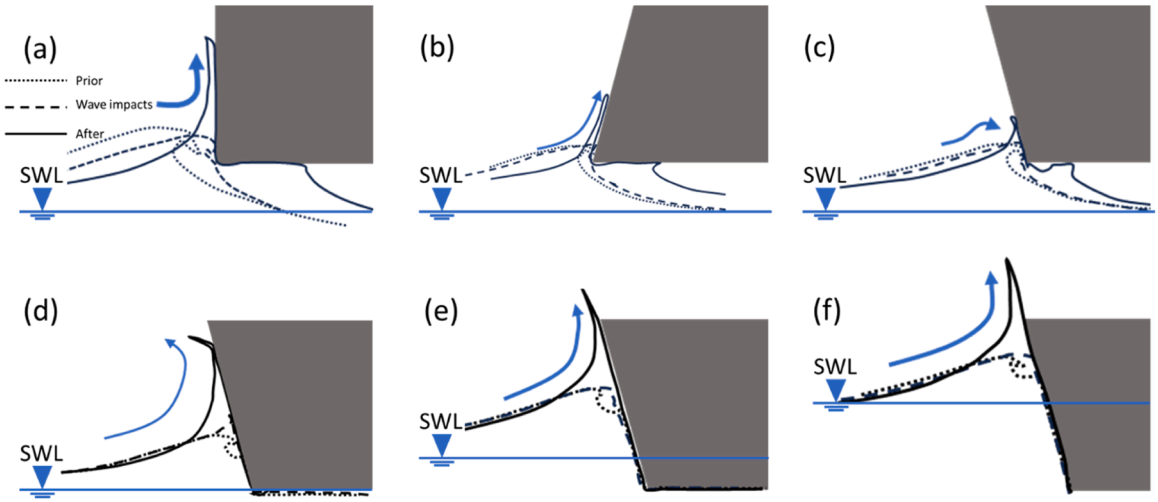

Fig. 18. Free surface tracer lines prior to breaking wave impact (dotted), as the wave impacts (dashed), and after the impact (solid) of (a) Vertical, (b) Positive 15°, and (c) Negative 15° cases of the fully elevated structure. For comparison, similarly arranged traced free surface movement of Negative 15° cases of SWL (d), semi-submerged (e), and on-grade (f) are presented. The blue arrow indicates the splash movement as it interacts with the structure, and the blue horizontal line indicate the SWL location.

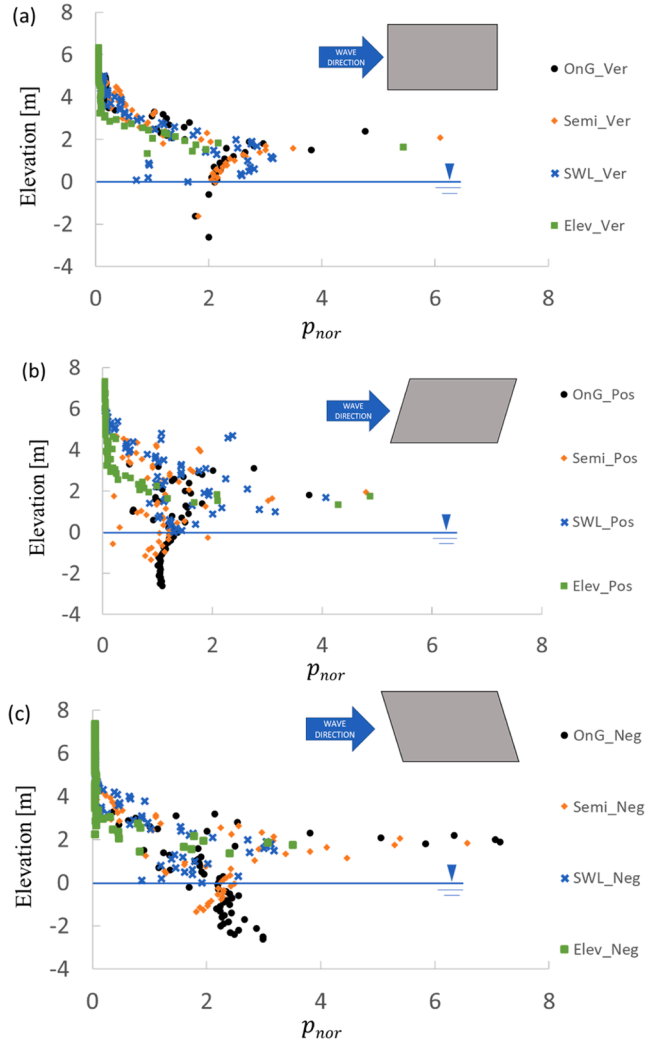

Fig. 19. Normalized peak presure maxima at various structure elevations for (a) Vertical wall, (b) Positive 15°, and (c) Negative 15°. Zero on y-axis indicates the SWL elevation.

$$\boldsymbol{F} = (\boldsymbol{F}_{tot})_{front}\cos\theta \tag{29}$$

and the vertical force per unit width (V) includes both the force acting on the bottom of the structure and the vertical component acting on the wall:

$$\boldsymbol{V} = (\boldsymbol{F}_{tot})_{bot} - (\boldsymbol{F}_{tot})_{front}\sin\theta \tag{30}$$

Fig. 20 compares the horizontal force per unit with (F) measured on the front face of the structure (y-axis) and the total vertical force per unit width (V) attracted by the structure (x-axis) for the semi-submerged, still-water level, and fully elevated cases. The force compared in this figure is calculated using Eq. (27)–(30) with p_n and $p_{(n+1)}$ referring to the peak pressure at two adjacent points (which may not occur at the same time), thus representing a hypothetical worst-case scenario. The On-Grade cases are not included in Fig. 20 because the bottom of the structure is touching the ground. Note that the influence of the structure's weight is omitted in the analysis and thus not considered in the vertical force calculation.

With the exception of structures elevated to the SWL, the total vertical and horizontal forces are similar across most of the cases due to their proximity to the 45-degree equivalence line. This observation is especially true for vertical walls. It is also interesting to observe that for semi-submerged cases, the ratio between vertical to horizontal forces

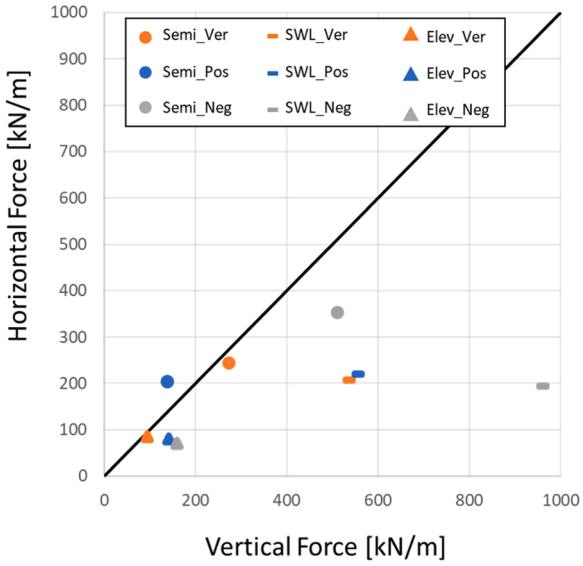

Fig. 20. Comparison of the total vertical (x-axis) and horizontal (y-axis) force attracted by the structure.

(V/F) increases as the angle of wall inclination shifts from positive to negative. The increase in total vertical force is likely due to the increased contribution of the vertical component of the force acting on the front wall given by $(F_{tot})_{front}\sin\theta$. This influence is more apparent in the semi-submerged case due to the high pressures experienced by the negatively inclined wall. Furthermore, the total vertical and horizontal forces are smallest for the fully elevated structure (despite a high localized peak pressure observed in Fig. 19a) and is consistent with past experimental observations (Park et al., 2017). Yet, the vertical forces attracted by the structure elevated above the SWL is greater than its horizontal counterpart with the largest vertical to horizontal force ratio observed for the negatively inclined wall.

An interesting phenomenon is observed for the still-water level cases where the vertical force is much larger than the horizontal force. These results are in line with the findings described in (Park et al., 2017), where the vertical force becomes greater than 5 times the horizontal when the structure is located at the SWL. Fig. 21 breaks down the flow visualization of the SWL_Ver case and explains this phenomenon. It can be seen that as the wave propagates to the location of the structure, a small air gap formed (Fig. 21b) due to set-down of the incoming wave. This air gap created a very high impact pressure experienced by the structure as the breaking wave's momentum continued to pass underneath leading to a high velocity upward jet at the back of the structure (Fig. 21c) and high vertical forces along the base.

It is further observed that the negative 15° orientation consistently gives the highest vertical force (relative to the horizontal) in all cases. This influence may happen because a negatively inclined front wall redirects the momentum of the wave downward towards the bottom of the structure thus reflecting less wave energy. This influence is understandably more significant in the case of semi-submerged and SWL elevations.

5.5. Void formation in SPH

The application of smoothed particle hydrodynamics for highly turbulent fluids exhibiting extreme deformations such as wave breaking has shown good levels of accuracy in previous studies (Lu et al., 2021). However, some interparticle instabilities may occur where voids form (an empty space with no particles) (Guilcher et al., 2013; Lu et al., 2021). Voids were observed to form for the elevated cases in this study with Fig. 22 demonstrating void development under the elevated structure with negative 15° inclination (the structure is bordered with a

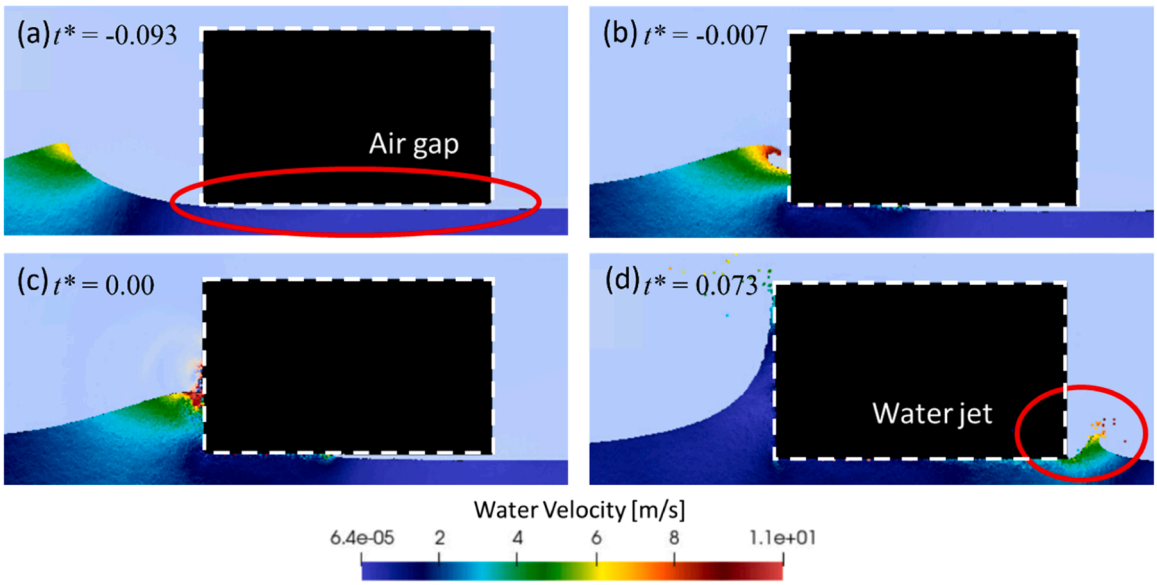

Fig. 21. Flow visuaization of the SWL_Ver case during (a) wave propagation toward the structure, (b) plunger formation, (c) impact, and (d) after impact with a water jet behind the structure circled in red.

dashed white line for clarity). In addition, Fig. 23 shows the corresponding time series pressure measurement at the bottom front corner of the structure. The letters (a) to (d) indicate the pressure measurement at each snapshot visualized in Fig. 22a to d.

Fig. 22a shows the breaking wave impacting the structure which is reflected in Fig. 23 as an initial pressure spike. As the wave crest propagates, a void develops under the structure between the water particles and the structure's border (circled in red in Fig. 22b). This void development occurred due to the downwards motion of water particles under the effect of gravity creating a barrier blocking the infiltration of air particles into the newly formed void.

In SPH, the pressure is calculated using the number of particles in a given area and their velocities. Since water particles are moving downwards, a fictitious negative pressure was recorded at this point as indicated in Fig. 23. Once a permeable gap is created between the water particles and the structure's border, air particles rush to fill in the lower pressure region (void) (Fig. 22c). This air particle movement created another fictitious high-pressure measurement as shown in Fig. 23 marked "Fig. 22(c)". Finally, the pressure returns to zero (atmospheric) once the air particles eliminated the void in Fig. 22d. This void formation is likely occurring due to only one plane being available for air particles to move to a lower pressure area in a 2D simulation. This void problem is thus unlikely to be found in 3D simulations, which might cost 100 to 120 times more computational power depending on the width of

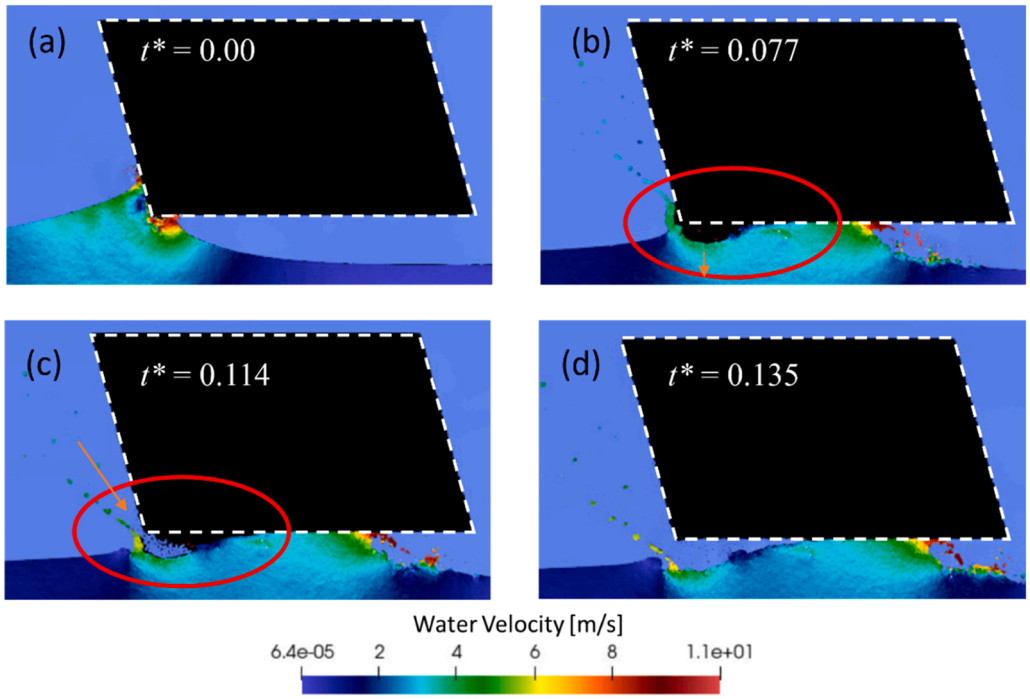

Fig. 22. Flow visualization of Elev_Neg during (a) breaking wave impacting the structure, (b) water particles moving downward due to gravity leading to a void (circled in red) developing, (c) air particles rushing to fill the void, and (d) wave contining to propagate below the structure.

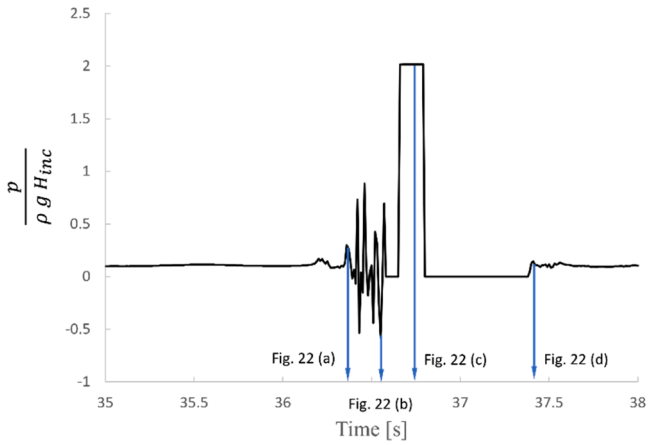

Fig. 23. Normalized presure time series measured at the front corner corresponding to the event demonstrated in Fig. 22a–d.

the 3D domain (Reis et al., 2022). For the total force calculation shown in Fig. 20, however, the influence of any voids on pressure measurement has been identified, analyzed, and removed to ensure the total vertical force calculated is comparable with the horizontal component on the front wall (where no voids were observed).

6. Summary and conclusions

The ever-increasing risk of coastal disasters due to climate change highlights the importance of improving coastal resilience. The current study examines elevated buildings during hurricane-induced flooding by exploring the influence of front wall inclination to breaking wave loads experienced by the structure. To achieve these objectives, a series of breaking wave impacts on an elevated coastal structure with its front wall inclined at different angles were implemented using the Lagrangian smoothed-particle hydrodynamics (SPH) method via the open-source program DualSPHysics. Prior to the parametric study, the numerical scheme was successfully validated against experimental results involving the generation of impact pressures from waves breaking on an inclined wall. The validation demonstrated that both single-phase and multiphase SPH simulation were able to simulate breaking wave impact, albeit with slight modification in the single-phase approach. Nevertheless, only the multiphase approach was deployed for current study since it was more accurately able to capture the short duration of impact pressures.

A 10 m long and 6 m high elevated structure (matching a typical two-story building) consistent with that examined experimentally by (Park et al., 2017) was adopted. Three front wall inclinations of negative 15°, 0° (vertical), and positive 15° were considered. These inclinations were paired with four structural elevations relative to the still-water level (SWL) of −2.7 m (On-Grade), −1.25 m (semi-submerged), 0 m (SWL), and 1.25 m (elevated). A summary of the results are as follows:

- *Influence of wall inclination* – When the bottom of the structure is located below the still water level, a positive 15° inclination on the front wall may reduce impact loads resulting from breaking waves up to 21 % relative to a vertical wall. A negative 15° inclination, on the other hand, revealed an increase in breaking wave impact pressures of up to 1.6 times that experienced by a vertical surface. When the base of the structure is elevated to the SWL, a positive 15° inclination increased the maximum pressure by a factor of 1.3 while the negative 15° case was comparable with the vertical wall. Finally, once the entire structure is elevated above the still water level, both positive and negative 15° inclinations reduced the maximum pressure on the front wall by a factor of 0.9 and 0.65, respectively, relative to the vertical surface.
- *Influence of structural elevation* – When comparing the same wall inclination across multiple structural elevations, the SWL elevation was found to give the lowest pressure peak on the front wall for all of the inclinations considered. In terms of the highest pressure experienced by the structure, the results varied depending on the wall inclination. For the vertical wall, the highest pressure was measured for the semi-submerged case, followed by the fully elevated case and then by the on-grade case. For the positive wall inclination, the highest pressure was comparable between the semi-submerged and the fully elevated case, which was followed by the on-grade case. When the wall was negatively inclined, the highest normalized pressure was recorded on both the On-Grade and semi-submerged case. A significant improvement is shown on the elevated case with about half of the pressure of the on-grade and semi-submerged cases.
- *Horizontal and vertical force comparison* – The total horizontal force experienced by the front wall of the structure and the total vertical force were relatively comparable with the exception of the SWL cases which observed much larger vertical forces. When the structure is elevated to the SWL, a small air gap developed between the water surface and the base immediately prior to wave impact (due to wave set-down) which then resulted in high impact pressures impacting the bottom of the structure.

Generally speaking, if the structure is either submerged or semi-submerged, positive wall inclinations are expected to reduce breaking wave impact loads. However, negative inclinations are observed to reduce impact pressures on structures elevated at or above the SWL.

For these studies, multiphase SPH correlated better with the experiments, which involved breaking wave impact, when compared with its single-phase counterpart. Care must be taken when simulating large deformation flows in 2D multiphase as artificial voids may form where air particles are blocked by the water particles. It is hypothesized that this issue may be ameliorated by employing 3D domains. Furthermore, the simulations in the current study are limited since the latest developments in the following have yet to be implemented in DualSPHysics v5.0,which was used in the current studies: the acoustic damper term in weakly compressible SPH (Sun et al., 2023), velocity-divergence error mitigating (VEM) scheme, and the volume conservation shifting (VCS) scheme (Khayyer et al., 2023). The implementation of these schemes can be attempted in future studies to increase the overall accuracy of multiphase simulations.

CRediT authorship contribution statement

Krisna Adi Pawitan: Conceptualization, Data curation, Formal analysis, Investigation, Methodology, Validation, Writing – original draft. **Maria Garlock:** Supervision, Conceptualization, Funding acquisition, Formal analysis, Writing – review & editing. **Shengzhe Wang:** Conceptualization, Supervision, Formal analysis, Writing – review & editing.

Declaration of Competing Interest

The authors declare that they have no known competing financial interests or personal relationships that could have appeared to influence the work reported in this paper.

Data availability

Data will be made available on request.

Acknowledgments

This research was sponsored by the National Science Foundation (NSF) under grant CMMI- 2227489. All opinions expressed in this paper

are the authors' and do not necessarily reflect the policies and views of the sponsors.

References

Allsop, N.W.H., McKenna, J.E., Vicinanza, D., Whittaker, T.T.J., 1996. New design methods for wave impact loadings on vertical breakwaters and seawalls. Coastal Eng. 2508–2521, 1996.

Altomare, C., Crespo, A.J., Domínguez, J.M., Gómez-Gesteira, M., Suzuki, T., Verwaest, T., 2015. Applicability of smoothed particle hydrodynamics for estimation of sea wave impact on coastal structures. Coastal Eng. 96, 1–12.

Altomare, C., Crespo, A.J., Rogers, B.D., Dominguez, J.M., Gironella, X., Gómez-Gesteira, M., 2014. Numerical modelling of Armour Block Sea breakwater with smoothed particle hydrodynamics. Comput. Struct. 130, 34–45.

Altomare, C., Gironella, X., Crespo, A.J., 2021. Simulation of random wave overtopping by a WCSPH model. Appl. Ocean Res. 116, 102888.

Altomare, C., Scandura, P., Cáceres, I., Viccione, G., 2023. Large-scale wave breaking over a barred beach: SPH numerical simulation and comparison with experiments. Coastal Eng. 185, 104362.

Batchelor, G.K., 1967. An Introduction to Fluid Dynamics. Cambridge university press.

Altomare, C., Domínguez, J.M., Crespo, A.J.C., González-Cao, J., Suzuki, T., Gómez-Gesteira, M., Troch, P., 2017. Long-crested wave generation and absorption for SPH-based DualSPHysics model. Coastal Eng. 127, 37–54.

Altomare, C., Domínguez, J.M., Fourtakas, G., 2022. Latest developments and application of SPH using dualSPHysics. Comput. Part. Mech. 9 (5), 863–866.

Bullock, G.N., Obhrai, C., Peregrine, D.H., Bredmose, H., 2007. Violent breaking wave impacts. Part 1: results from large-scale regular wave tests on vertical and sloping walls. Coastal Eng. 54 (8), 602–617.

Cooker, M.J., 2002. Liquid impact, kinetic energy loss and compressibility: lagrangian, Eulerian and acoustic viewpoints. J. Eng. Math. 44, 259–276.

Cooker, M.J., Peregrine, D.H., 1992. Wave impact pressure and its effect upon bodies lying on the sea bed. Coastal Eng. 18 (3–4), 205–229.

Crespo, A.J., Domínguez, J.M., Rogers, B.D., Gómez-Gesteira, M., Longshaw, S., Canelas, R.J.F.B., Vacondio, R., Barreiro, A., García-Feal, O., 2015. DualSPHysics: open-source parallel CFD solver based on smoothed particle hydrodynamics (SPH). Comput. Phys. Commun. 187, 204–216.

Cuomo, G., Allsop, W., Bruce, T., Pearson, J., 2010a. Breaking wave loads at vertical seawalls and breakwaters. Coastal Eng. 57 (4), 424–439.

Cuomo, G., Allsop, W., Takahashi, S., 2010b. Scaling wave impact pressures on vertical walls. Coastal Eng. 57 (6), 604–609.

Cuomo, G., Piscopia, R., Allsop, W., 2011. Evaluation of wave impact loads on caisson breakwaters based on joint probability of impact maxima and rise times. Coastal Eng. 58 (1), 9–27.

Domínguez, J.M., Fourtakas, G., Altomare, C., Canelas, R.B., Tafuni, A., García-Feal, O., Martínez-Estévez, I., Mokos, A., Vacondio, R., Crespo, A.J., Rogers, B.D., 2022. DualSPHysics: from fluid dynamics to multiphysics problems. Comput. Part. Mech. 9 (5), 867–895.

Domínguez, J.M., Altomare, C., Gonzalez-Cao, J., Lomonaco, P., 2019a. Towards a more complete tool for coastal engineering: solitary wave generation, propagation and breaking in an SPH-based model. Coastal Eng. J. 61 (1), 15–40.

Domínguez, J.M., Crespo, A.J., Hall, M., Altomare, C., Wu, M., Stratigaki, V., Troch, P., Cappietti, L., Gómez-Gesteira, M., 2019b. SPH simulation of floating structures with moorings. Coastal Eng. 153, 103560.

English, A., Domínguez, J.M., Vacondio, R., Crespo, A.J.C., Stansby, P.K., Lind, S.J., Chiapponi, L., Gómez-Gesteira, M., 2022. Modified dynamic boundary conditions (mDBC) for general-purpose smoothed particle hydrodynamics (SPH): application to tank sloshing, dam break and fish pass problems. Comput. Part. Mech. 9 (5), 1–15.

Fourtakas, G., Dominguez, J.M., Vacondio, R., Rogers, B.D., 2019. Local uniform stencil (LUST) boundary condition for arbitrary 3-D boundaries in parallel smoothed particle hydrodynamics (SPH) models. Comput. Fluids 190, 346–361.

Fourtakas, G., Vacondio, R., Alonso, J.D., Rogers, B.D., 2020. Improved density diffusion term for long duration wave propagation. In: Proceedings of the SPHERIC Harbin International Workshop.

Fox-Kemper, B., Hewitt, H.T., Xiao, C., Aðalgeirsdóttir, G., Drijfhout, S.S., Edwards, T.L., et al., 2021. Ocean, Cryosphere and sea level change. In: Masson-Delmotte, V., Zhai, P., Pirani, A., Connors, S.L., Péan, C., Berger, S., et al. (Eds.), Climate change 2021: The physical science basis. Contribution of working Group I to the sixth assessment report of the intergovernmental panel on climate change. Cambridge University Press.

Fuhrboter, A., 1968. Laboratory investigation of impact forces. In: Proceedings of the Symposium on Research on Wave Action, II. Delft Hydraulic Laboratory.

Guilcher, P.M., Couty, N., Brosset, L., Le Touzé, D., 2013. Simulations of breaking wave impacts on a rigid wall at two different scales with a two-phase fluid compressible SPH model. Int. J. Offshore Polar Eng. 23 (04), 241–253.

Heller, V., Bruggemann, M., Spinneken, J., Rogers, B.D., 2016. Composite modelling of subaerial landslide–tsunamis in different water body geometries and novel insight into slide and wave kinematics. Coastal Eng. 109, 20–41.

Hughes, S.A., 1993. Physical Models and Laboratory Techniques in Coastal Engineering, 7. World Scientific.

Khayyer, A., Shimizu, Y., Gotoh, T., Gotoh, H., 2023. Enhanced resolution of the continuity equation in explicit weakly compressible SPH simulations of incompressible free-surface fluid flows. Appl. Math. Model. 116, 84–121.

Khayyer, A., Gotoh, H., Shimizu, Y., 2017. Comparative study on accuracy and conservation properties of two particle regularization schemes and proposal of an optimized particle shifting scheme in ISPH context. J. Comput. Phys. 332, 236–256.

Khayyer, A., Gotoh, H., 2016. A multiphase compressible-incompressible particle method for water slamming. Int. J. Offshore Polar Eng. 26 (01), 20–25.

Kirkgöz, M.S., 1991. Impact pressure of breaking waves on vertical and sloping walls. Ocean Eng. 18 (1–2), 45–59.

Le Méhauté, B., 2013. An Introduction to Hydrodynamics and Water Waves. Springer Science & Business Media.

Lichtenwalner, S., 2023. Significant Waves. March 15. Ocean Data Labs. Retrieved July 18, 2023from. https://datalab.marine.rutgers.edu/2013/03/significant-waves/.

Lind, S.J., Fang, Q., Stansby, P.K., Rogers, B.D., Fourtakas, G., 2017. A two-phase incompressible-compressible (water-air) Smoothed Particle Hydrodynamics (ICSPH) method applied to focused wave slam on decks. In: Proceedings of the ISOPE International Ocean and Polar Engineering Conference. ISOPE. ISOPE-I.

Lind, S.J., Xu, R., Stansby, P.K., Rogers, B.D., 2012. Incompressible smoothed particle hydrodynamics for free-surface flows: a generalised diffusion-based algorithm for stability and validations for impulsive flows and propagating waves. J. Comput. Phys. 231 (4), 1499–1523.

Liu, M.B., Liu, G., 2010. Smoothed particle hydrodynamics (SPH): an overview and recent developments. Arch. Comput. Methods Eng. 17, 25–76.

Liu, S., Gatin, I., Obhrai, C., Ong, M.C., Jasak, H., 2019. CFD simulations of violent breaking wave impacts on a vertical wall using a two-phase compressible solver. Coastal Eng. 154, 103564.

Lu, X., Cherfils, J.M., Pinon, G., Rivoalen, E., Kimmoun, O., Brossard, J., 2021. SPH numerical computations of wave impact onto a vertical wall with experimental comparisons. C. R. Méc. 349 (1), 117–143.

Marrone, S., Colagrossi, A., Baudry, V., Le Touzé, D., 2019. Extreme wave impacts on a wave energy converter: load prediction through a SPH model. Coastal Eng. J. 61 (1), 63–77.

Meringolo, D.D., Colagrossi, A., Marrone, S., Aristodemo, F., 2017. On the filtering of acoustic components in weakly-compressible SPH simulations. J. Fluids Struct. 70, 1–23.

Mitsuyasu, H., 1966. Shock pressure of breaking wave. Coastal Eng. 268–283, 1966.

Mokos, A., Rogers, B.D., Stansby, P.K., 2017. A multi-phase particle shifting algorithm for SPH simulations of violent hydrodynamics with a large number of particles. J. Hydraul. Res. 55 (2), 143–162.

Monaghan, J.J., 1992. Smoothed particle hydrodynamics. Annu. Rev. Astron. Astrophys. 30 (1), 543–574.

Monaghan, J.J., 1994. Simulating free surface flows with SPH. J. Comput. Phys. 110 (2), 399–406.

Monaghan, J.J., Cas, R.A., Kos, A.M., Hallworth, M., 1999. Gravity currents descending a ramp in a stratified tank. J. Fluid Mech. 379, 39–69.

Monaghan, J.J., 2005. Smoothed particle hydrodynamics. Rep. Prog. Phys. 68, 1703–1759.

Müller, G.U., Whittaker, T.J.T., 1993. An investigation of breaking wave pressures on inclined walls. Ocean Eng. 20 (4), 349–358.

Nagai, S., 1960. Shock pressures exerted by breaking waves on breakwaters. J. Waterw. Harb. Div. 86 (2), 1–38.

Nugent, S., Posch, H.A., 2000. Liquid drops and surface tension with smoothed particle applied mechanics. Phys. Rev. E Stat. Phys. Plasmas Fluids Relat. Interdiscip. Top. 62 (4), 4968–4975. Pt A.

Oumeraci, H., 1994. Review and analysis of vertical breakwater failures—Lessons learned. Coastal Eng. 22 (1–2), 3–29.

Oumeraci, H., Klammer, P., Partenscky, H.W., 1993. Classification of breaking wave loads on vertical structures. J. Waterw. Port Coast. Ocean Eng. 119 (4), 381–397.

Park, H., Tomiczek, T., Cox, D.T., van de Lindt, J.W., Lomonaco, P., 2017. Experimental modeling of horizontal and vertical wave forces on an elevated coastal structure. Coastal Eng. 128, 58–74.

Pawitan, K.A., Dimakopoulos, A.S., Vicinanza, D., Allsop, W., Bruce, T., 2019. A loading model for an OWC caisson based upon large-scale measurements. Coastal Eng. 145, 1–20.

Pawitan, K.A., Vicinanza, D., Allsop, W., Bruce, T., 2020. Front wall and in-chamber impact loads on a breakwater-integrated oscillating water column. J. Waterw. Port Coast. Ocean Eng. 146 (5), 04020037.

Peregrine, D.H., 2003. Water wave impacts on walls. Annu. Rev. Fluid Mech. 35, 23–43.

Reis, C., Barbosa, A.R., Figueiredo, J., Clain, S., Lopes, M., Baptista, M.A., 2022. Smoothed particle hydrodynamics modeling of elevated structures impacted by tsunami-like waves. Eng. Struct. 270, 114851.

Richert, G., 1968. Experimental investigation of shock pressures against breakwaters. Coastal Eng. 954–973, 1968.

Rogers, B.D., Dalrymple, R.A., Stansby, P.K., 2010. Simulation of caisson breakwater movement using 2-D SPH. J. Hydraul. Res. 48 (sup1), 135–141.

Roselli, R.A.R., Vernengo, G., Altomare, C., Brizzolara, S., Bonfiglio, L., Guercio, R., 2018. Ensuring numerical stability of wave propagation by tuning model parameters using genetic algorithms and response surface methods. Environ. Model. Softw. 103, 62–73.

Sato, K., Kawasaki, K., Watanabe, K., Koshimura, S., 2021. Validation of the applicability of the particle-based open-source software DualSPHysics to violent flow fields. Coastal Eng. J. 63 (4), 545–572.

Shimizu, Y., Khayyer, A., Gotoh, H., Nagashima, K., 2020. An enhanced multiphase ISPH-based method for accurate modeling of oil spill. Coastal Eng. J. 62 (4), 625–646.

Sun, P.N., Luo, M., Le Touzé, D., Zhang, A., 2019. The suction effect during freak wave slamming on a fixed platform deck: smoothed particle hydrodynamics simulation and experimental study. Phys. Fluids 31 (11).

Sun, P.N., Pilloton, C., Antuono, M., Colagrossi, A., 2023. Inclusion of an acoustic damper term in weakly-compressible SPH models. J. Comput. Phys. 483, 112056.

Suzuki, T., Altomare, C., Veale, W., Verwaest, T., Trouw, K., Troch, P., Zijlema, M., 2017. Efficient and robust wave overtopping estimation for impermeable coastal structures in shallow foreshores using SWASH. Coastal Eng. 122, 108–123.

Tomiczek, T., Prasetyo, A., Mori, N., Yasuda, T., Kennedy, A., 2016a. Physical modelling of tsunami onshore propagation, peak pressures, and shielding effects in an urban building array. Coast. Eng. 117, 97–112.

Tomiczek, T., Prasetyo, A., Mori, N., Yasuda, T., Kennedy, A., 2016b. Effects of a macroroughness element on tsunami wave amplification, pressures, and loads: physical model and comparison to Japanese and US designs. Coast. Eng. J. https://doi.org/10.1142/S0578563417500048.

Viviano, A., Naty, S., Foti, E., 2018. Scale effects in physical modelling of a generalized OWC. Ocean Eng. 162, 248–258.

Violeau, D., Rogers, B.D., 2016. Smoothed particle hydrodynamics (SPH) for free-surface flows: past, present and future. J. Hydraul. Res. 54 (1), 1–26.

Wang, S., Garlock, M., Deike, L., Glisic, B., 2022. Feasibility of Kinetic Umbrellas as deployable flood barriers during landfalling hurricanes. J. Struct. Eng. 148 (5), 04022047.

Wehner, M., Seneviratne, S., Zhang, X., Adnan, M., Badi, W., Dereczynski, C., Di Luca, A., Ghosh, S., Iskandar, I., Kossin, J., Lewis, S., 2021. Weather and climate extreme events in a changing climate. In: Proceedings of the AGU Fall Meeting Abstracts, 2021, pp. U13B–U111.

Wendland, H., 1995. Piecewise polynomial, positive definite and compactly supported radial functions of minimal degree. Adv. Comput. Math. 4, 389–396.

Whillock, A.F., 1987. Measurements of forces resulting from normal and oblique wave approaches to small scale sea walls. Coastal Eng. 11 (4), 297–308.